

A LARGE-FIELD $J = 1 - 0$ SURVEY OF CO AND ITS ISOTOPOLOGUES TOWARD THE CASSIOPEIA A
SUPERNOVA REMNANT

YUEHUI MA,^{1,2} HONGCHI WANG,¹ MIAOMIAO ZHANG,¹ CHONG LI,^{1,2} AND JI YANG¹

¹*Purple Mountain Observatory and Key Laboratory of Radio Astronomy, Chinese Academy of Sciences, 2 West Beijing Road, Nanjing 210008, China*

²*University of Chinese Academy of Sciences, 19A Yuquan Road, Shijingshan District, Beijing 100049, China*

Submitted to ApJ

ABSTRACT

We have conducted a large-field simultaneous survey of ^{12}CO , ^{13}CO , and C^{18}O $J = 1 - 0$ emission toward the Cassiopeia A (Cas A) supernova remnant (SNR), which covers a sky area of $3.5^\circ \times 3.1^\circ$. The Cas giant molecular cloud (GMC) mainly consists of three individual clouds with masses on the order of $10^4 - 10^5 M_\odot$. The total mass derived from the ^{13}CO emission of the GMC is $2.1 \times 10^5 M_\odot$ and is $9.5 \times 10^5 M_\odot$ from the ^{12}CO emission. Two regions with broadened ($6 - 7 \text{ km s}^{-1}$) or asymmetric ^{12}CO line profiles are found in the vicinity (within a $10' \times 10'$ region) of the Cas A SNR, indicating possible interactions between the SNR and the GMC. Using the GAUSSCLUMPS algorithm, 547 ^{13}CO clumps are identified in the GMC, 54% of which are supercritical (i.e. $\alpha_{\text{vir}} < 2$). The mass spectrum of the molecular clumps follows a power-law distribution with an exponent of -2.20 . The pixel-by-pixel column density of the GMC can be fitted with a log-normal probability distribution function (N-PDF). The median column density of molecular hydrogen in the GMC is $1.6 \times 10^{21} \text{ cm}^{-2}$ and half the mass of the GMC is contained in regions with H_2 column density lower than $3 \times 10^{21} \text{ cm}^{-2}$, which is well below the threshold of star formation. The distribution of the YSO candidates in the region shows no agglomeration.

Keywords: ISM: clouds — ISM: individual objects(Cas A) — ISM: supernova remnants — stars: formation — surveys

arXiv:1905.10193v1 [astro-ph.GA] 24 May 2019

1. INTRODUCTION

Molecular clouds are the densest part of the interstellar medium and the birthplace of stars. Although molecular hydrogen (H_2) is the primary component of molecular clouds, they are difficult to observe via rotational transition lines as H_2 possesses no permanent dipole moment. The most commonly used tracers of molecular clouds are the ^{12}CO molecule and its isotopologues. In the past four decades, there have been plenty of large-scale CO surveys of the Milky Way (for a review, see Heyer & Dame (2015)), such as the most extensive CfA-Chile survey (Dame et al. 2001) and the FCRAO Outer Galaxy Survey (OGS) (Heyer et al. 2001). These surveys revealed the global distribution and statistical properties of molecular gas in the Milky Way. The majority of molecular clouds are accumulated into cloud complexes, which are called giant molecular clouds (GMCs). The sizes and masses of GMCs lie approximately in the range from 10 to 150 pc and $10^3 M_\odot$ to $10^7 M_\odot$, respectively. GMCs are composed of hierarchical structures like clouds, clumps, and cores (Scalo 1985; Falgarone & Perault 1987; Blitz & Williams 1999). The mass function of molecular clouds follows a power law, with distinct power-law exponents for the inner and the outer Galaxy, -1.6 and -2.2 , respectively (Rice et al. 2016). There exists a scaling relation between the line-widths and the sizes of molecular clouds over a wide range of cloud size (Larson 1981; Solomon et al. 1987). Turbulence is considered to be one of the origins of this line-width-size relation and the hierarchical structure of molecular clouds (Vazquez-Semadeni 1994). The physical properties and dynamical state of molecular clumps are of great importance as molecular clumps are observed to be the birthplace of massive clusters (Williams et al. 1995). Different statistical properties are expected for clumps under different supporting and confining mechanisms (Bertoldi & McKee 1992; Heyer et al. 2001; Kauffmann et al. 2013). In addition, the temperature and number density of molecular clumps also vary with different interstellar environments (Blitz 1993; Williams et al. 1995).

The structure and dynamics of molecular clouds are strongly influenced by dynamical processes like cloud–cloud collision, stellar winds from massive stars, and supernova explosion (Truelove & McKee 1999; Matzner 2002; Bally 2016), among which the supernova explosion is the most intense. The blast wave of the explosion drives strong shocks into the surrounding interstellar medium. When the shock hits a molecular cloud, the shocked gas will be compressed, accelerated, and heated, leading to a variety of observable effects such as OH 1720 MHz maser emission, velocity broad-

ening of the molecular-line emission, extended wing emission of ^{12}CO low- J transition lines, or high CO $J = 2 - 1/J = 1 - 0$ line intensity ratio (Seta et al. 1998; Jiang et al. 2010). However, among the 295 supernova remnants (SNRs) detected in the Milky Way (Green 2017), only $\sim 23\%$ of them are confirmed or suggested to be associated with molecular clouds (Jiang et al. 2010; Chen et al. 2014).

The Cassiopeia A SNR is the youngest known supernova remnant in our Galaxy and is the brightest discrete radio source at 100–1000 MHz in the sky, except for our Sun. It is the outcome of a Type IIb supernova explosion at around 1681 A.D. (Fesen et al. 2006; Krause et al. 2008). The morphological structures, physical properties, and chemical compositions of the Cas A SNR have been studied by many multiband observations. The SNR is mainly composed of a broken shell of size $\sim 4'$ as observed in the X-ray, optical, and IR wavelengths. The main shell consists of the reverse shocked debris that is rich of O, Si, S, Ar, and Ca elements (Thorstensen et al. 2001). Furthermore, a lot of “fast-moving knots (FMKs)” are distributed asymmetrically along the northeast and southwest directions (Reed et al. 1995; Thorstensen et al. 2001; Ennis et al. 2006; Patnaude & Fesen 2014). The outermost FMKs are located beyond the forward shock ($\sim 5'$ in diameter) and have expansion velocities greater than $\sim 10,000 \text{ km s}^{-1}$ (Fesen & Gunderson 1996; Gotthelf et al. 2001; Fesen et al. 2006; Hammell & Fesen 2008). Optical spectroscopic observations of the FMKs revealed that the Cas A SNR is located at the distance of $3.4^{+0.3}_{-0.1} \text{ kpc}$ (Reed et al. 1995).

There have been many studies on the relationship between the Cas A SNR and the surrounding medium. X-ray observations reveal that Cas A is expanding in the wind of its progenitor star (Lee et al. 2014). The flickering and trailing emissions of the optical knots in the remnant’s periphery indicate the initial stage of the interactions between the SN ejecta and the surrounding ISM (Fesen et al. 2011). Absorption lines of the molecules OH, H_2CO , and HCO^+ (Goss et al. 1984; Bieging & Crutcher 1986; Reynoso & Goss 2002; Zhou et al. 2018), and emission lines of CO and its isotopologues have been detected toward the SNR (Wilson et al. 1993; Kilpatrick et al. 2014; Zhou et al. 2018). These observations have shown that some molecular gas of the GMC coincides with the SNR along the line of sight. However, whether there is any interaction between the SNR and the molecular gas is still unclear. A supporting evidence for the interaction is the slightly broadened H_2CO lines found by Reynoso & Goss (2002) and the broadened $^{12}\text{CO } J = 2 - 1$ lines found by Kilpatrick

et al. (2014). Recently, Zhou et al. (2018) suggested that there is no distinctive physical evidence for an interaction between the Cas A SNR and molecular gas. Observations by both Kilpatrick et al. (2014) and Zhou et al. (2018) are limited to a sky coverage of only or less than $10' \times 10'$ centered on the SNR. Wide-field surveys of molecular gas around the Cas A SNR include the CfA-Chile survey (Dame et al. 2001) and the FCRAO OGS survey (Heyer et al. 1998). Ungerechts et al. (2000) have provided an $\sim 8^\circ \times 8^\circ$ map of the GMCs in the region of Cas A and NGC 7538 as part of the CfA-Chile survey, but the mapping has quite coarse resolution and low sensitivity. The FCRAO OGS survey has only partly covered the MCs around Cas A (see Figure 1 in Heyer et al. 2001). Therefore, a detailed study of the structures and physical properties of the molecular gas toward the Cas A SNR is still lacking.

In this work, we present a large-scale ($3.5^\circ \times 3.1^\circ$) survey of molecular gas toward the Cas A SNR, as part of the MWISP project¹ (Su et al. 2019). The observation is described in Section 2 and the results are presented in Section 3. We discuss the column density distribution and star formation activity in this region in Section 4 and give our summary in Section 5.

2. OBSERVATIONS

The observations were taken using the PMO-13.7 m millimeter-wavelength telescope located at Delingha in China during two observational seasons from 2015 October to 2016 April and 2016 October to 2017 April. The $^{12}\text{CO } J = 1 - 0$, $^{13}\text{CO } J = 1 - 0$, and $\text{C}^{18}\text{O } J = 1 - 0$ line emission data were obtained simultaneously through the nine-beam Superconducting Spectroscopic Array Receiver (SSAR) mounted on the telescope (Shan et al. 2012). The front end of the receiver is a two-sideband Superconductor-Insulator-Superconductor (SIS) mixer. The $^{12}\text{CO } J = 1 - 0$ line emission is contained in the upper sideband while $^{13}\text{CO } J = 1 - 0$ and $\text{C}^{18}\text{O } J = 1 - 0$ line emission in the lower sideband. The backend of the receiver is a Fast Fourier Transform Spectrometer (FFTS) with a total bandwidth of 1 GHz and 16,384 frequency channels, providing a spectral resolution of 61 kHz per channel. The resulting velocity resolution at 110 GHz is 0.17 km s^{-1} . During all the observational epochs, the half-power beam width (HPBW) of the telescope is about $52''$ and $50''$ at 110 GHz and 115 GHz, respectively. The pointing of the telescope has an accuracy of about $5''$. The antenna temperature is calibrated according to $T_{\text{mb}} = T_{\text{A}}^* / \eta_{\text{mb}}$ during the data collection process, where the main beam efficiency is 0.55 at 110

GHz and 0.51 at 115 GHz according to the status report² of the PMO-13.7 m millimeter telescope.

In the MWISP project, the sky area is divided into $30' \times 30'$ cells. For each cell, the observations were made in the position-switch on-the-fly (OTF) mode along the directions of the galactic longitude and galactic latitude, with a scanning rate of $50''$ per second and a dump time of 0.3 s. The MWISP pipeline uses the GILDAS/CLASS³ software package to reduce the data. This process includes the subtraction of a first-order baseline from each spectrum and the combination of the spectra for the same sky position obtained at different times. For each cell, the data are then regridded into $30'' \times 30''$ pixels in the directions of the galactic longitude and latitude. The final RMS noise level is $\sim 0.5 \text{ K}$ per channel at the $^{12}\text{CO } J = 1 - 0$ line wavelength and $\sim 0.3 \text{ K}$ at the $^{13}\text{CO } J = 1 - 0$ and $\text{C}^{18}\text{O } J = 1 - 0$ line wavelengths.

3. RESULTS

3.1. Spatial Distribution and Physical Properties of Cas GMC

3.1.1. Spatial Distribution

The average spectrum of the observed $3.5^\circ \times 3.1^\circ$ region is shown in Figure 1. There are mainly two velocity components in this region, one from -60 to -20 km s^{-1} and the other from -10 to 10 km s^{-1} . The first component is much stronger than the second one. Obviously, the second component is located in the solar neighborhood. In this work, we concentrate on the first component and the study on the second component is deferred to a future paper.

Figure 2 illustrates the spatial distribution of the integrated intensity of the ^{12}CO , ^{13}CO , and $\text{C}^{18}\text{O } J = 1 - 0$ emission. The blue, green, and red colors correspond to the ^{12}CO , ^{13}CO , and $\text{C}^{18}\text{O } J = 1 - 0$ integrated intensity, respectively. The integrated velocity range for both ^{12}CO and ^{13}CO is from -60 to -24.5 km s^{-1} . Only spectra having at least five contiguous channels with brightness temperature above $1.5 \sigma_{\text{rms}}$ are used for the intensity integration. For C^{18}O , the integrated velocity range is from -40 to -30 km s^{-1} with the same criterion as above. The known SNRs and H II regions in the region (Anderson et al. 2014; Green 2014; Massaro et al. 2015) are indicated with red circles. As can be seen from Figure 2, the ^{12}CO and ^{13}CO emission in this region appears to be clumpy, and throughout the whole GMC, the C^{18}O emission is very weak. In the following

¹ <http://www.radioast.nsd.cas.cn/mwisp.php>

² <http://english.dlh.pmo.cas.cn/fs/>

³ <http://www.iram.fr/IRAMFR/GILDAS>

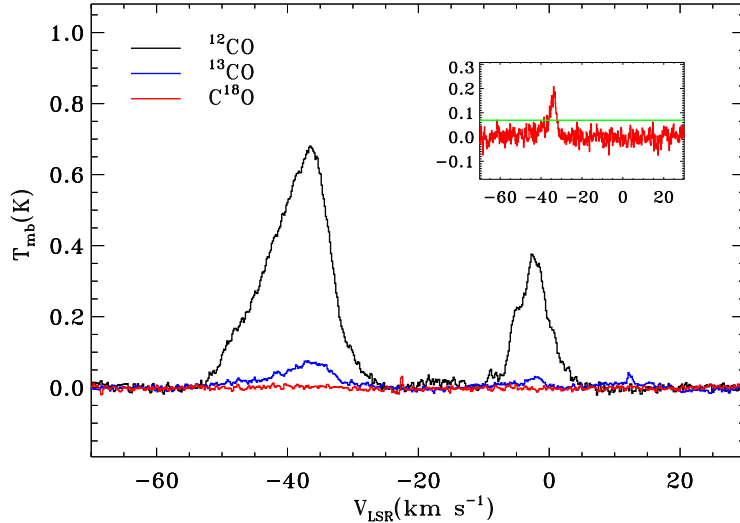


Figure 1. Average spectrum of the observed $3.5^\circ \times 3.1^\circ$ region. Black, blue, and red lines indicate the ^{12}CO , ^{13}CO , and C^{18}O $J = 1 - 0$ emission, respectively. The zoomed-in panel shows the average of the C^{18}O spectra that have at least four contiguous channels with C^{18}O emission above 1.5σ . The green line shows the 3σ noise level of the average spectrum. The emission of ^{13}CO at 13 km s^{-1} and the emission of C^{18}O at -22.5 km s^{-1} are due to bad channels.

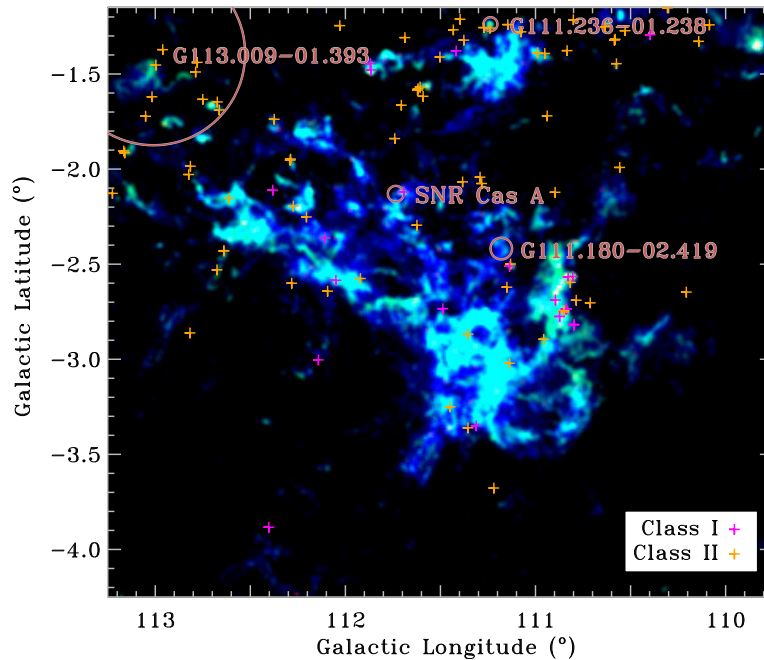


Figure 2. Composite map of the ^{12}CO , ^{13}CO , and C^{18}O $J = 1 - 0$ integrated intensity of the Cas GMC. The integrated velocity range is $[-60, -24.5] \text{ km s}^{-1}$ for the ^{12}CO and ^{13}CO emission and $[-40, -30] \text{ km s}^{-1}$ for C^{18}O . The blue, green, and red colors correspond to ^{12}CO , ^{13}CO , and C^{18}O emission, respectively. The Cas A SNR and the three H II regions from the WISE catalog (Anderson et al. 2014) in the region are indicated with red circles. The sizes of these circles correspond to their angular sizes. The Class II YSOs and Class I protostars identified in this work are marked with orange and magenta pluses, respectively.

analysis and calculation of this work, we only use the ^{12}CO and ^{13}CO data. Morphologically, there are two main separated substructures in this area, the north-

ern one with a meniscus shape below the H II region G111.236-01.238 and the southern one that consists of two filaments extending from the northeast to the south-

west with two shell-like structures at their southwestern ends. The Cas A SNR is located at the center of the north filament, while the H II region G113.009–01.393 is located near the northern end of this filament and the H II region G111.180–02.419 is associated with the shell-like structure.

Figure 3 displays the channel maps of the Cas GMC. We can see that the northern meniscus-shape cloud has velocity in the range from -45.5 to -33.5 km s^{-1} while the southern part of the Cas GMC exhibits two velocity components. The first component ranges from -54.5 to -43.5 km s^{-1} and is most discernible at the velocity channel -46.5 km s^{-1} . The second velocity component starts from -44.5 km s^{-1} and ends at -26.5 km s^{-1} . Therefore, from the spatial distribution and the velocity structure, we can see that the Cas GMC can be divided into three major clouds: Cloud 1 near the H II region G111.236–01.238 with a meniscus shape, Cloud 2 in the southern structure in the velocity range from -54.5 to -43.5 km s^{-1} , and Cloud 3 in the southern structure in the velocity range from -44.5 to -26.5 km s^{-1} . The channel maps of ^{13}CO emission in the region are presented in Figure 16 in the Appendix.

The position-velocity diagrams of the ^{12}CO emission of the Cas GMC are present in Figure 4. Figure 4(a) displays the l-v diagram, and Figure 4(b) displays the b-v diagram. The purple dashed line in Figure 4(a) shows the velocity of the Perseus Arm of model A5 from Reid et al. (2014). We can see that the majority of the Cas GMC has velocities consistent with the Perseus Arm, which suggests that the Cas GMC is located in the Perseus Arm. No distinct structures can be identified in the l-v diagram. It appears that there are velocity broadenings near the galactic longitudes of the H II regions G111.236–01.238 and G111.180–02.419. In fact, we find these velocity broadenings are caused by the velocity difference between Cloud 2 and Cloud 3. No velocity broadening is identified near the Cas A SNR or the H II region G113.009–01.393. In contrast to Figure 4(a), three distinct structures that correspond to Clouds 1-3 can be identified in the b-v diagram. As in the l-v diagram, no velocity broadening is found near the SNR or the H II regions. For comparison, the p-v diagrams of the ^{13}CO emission are presented in Figure 17 in the Appendix. From the b-v diagram of the ^{13}CO emission, we can see a ring structure in the southern end of Cloud 3 at $b = -3.1^\circ$ with velocity from -45 to -33 km s^{-1} . This ring coincides with the shell-like structure located at $[l, b] = [111.3, -3.0]^\circ$, as seen clearly in the -46.5 to -41.5 km s^{-1} panels in Figure 3. A ring structure in a p-v diagram is often considered to be an expanding sphere (Arce et al. 2011). In this case, however, we have

not found any source in the region that is responsible for the expansion.

The centroid velocity and the velocity dispersion maps of the ^{12}CO emission are presented in Figure 5. As shown in Figure 5(a), although Clouds 2 and 3 somewhat coincide in spatial distribution, they exhibit distinct velocities with Cloud 2 shown in blue and Cloud 3 in yellow and orange. The southwestern and northeastern ends of Cloud 3 show red-shift velocities. In Figure 5(b), we can see that large velocity dispersions (>3.5 km s^{-1}) are mostly due to the spatial coincidence of Clouds 2 and 3. In order to examine the velocity dispersion of individual clouds, we separate Cloud 2 from Cloud 3, and present their velocity dispersion maps in Figure 6. The median velocity dispersion of the ^{12}CO emission is about 0.6 km s^{-1} for Cloud 2 and 1.3 km s^{-1} for Cloud 3. No apparent line broadening exists near the three H II regions. A clump with large velocity dispersions (up to 4 km s^{-1}) can be found to the east of the Cas A SNR in Cloud 3.

3.1.2. Physical Properties

Following the method of Heyer et al. (2001), the centroid position, $[l_c, b_c, v_c]$, of a cloud that occupies N voxels in PPV space can be calculated through $\mathbf{x}_c = \Sigma_{i=1}^N T_i \mathbf{x}_i / \Sigma_{i=1}^N T_i$, where \mathbf{x} refers to l , b , or v and T_i is the brightness temperature of voxel i . The equivalent line width of a cloud can be obtained from the composite spectrum by dividing its integrated intensity by its emission peak. For the calculation, we only use the spectra that have at least five contiguous channels with brightness temperatures above 1.5σ . Based on the derived centroid position, the kinematic distance, d_k , of a cloud can be obtained under the assumption of a flat rotation curve of the Galaxy (we use model A5 of Reid et al. 2014 in this work).

The measured centroid positions and kinematic distances of Clouds 1–3 are listed in Table 1. The kinematic distances of Clouds 1–3 are 3.17, 3.73, and 3.00 kpc, respectively. We can see that the velocity and distance of Cloud 2 are not consistent with those of Clouds 1 and 3. We checked the trigonometric parallax distances of the two galactic masers, G111.23–01.23 and G111.25–00.76, which are located in or adjacent to the observed region. The parallax distances of G111.23–01.23 and G111.25–00.76, 3.472 and 3.401 kpc respectively (Reid et al. 2014), are consistent with each other, although their radial velocity difference amounts to 10 km s^{-1} (-53 km s^{-1} for maser G111.23–01.23 and -43 km s^{-1} for maser G111.25–00.76). Considering the non-circular motion of the Milky Way and the intrinsic velocity dispersions

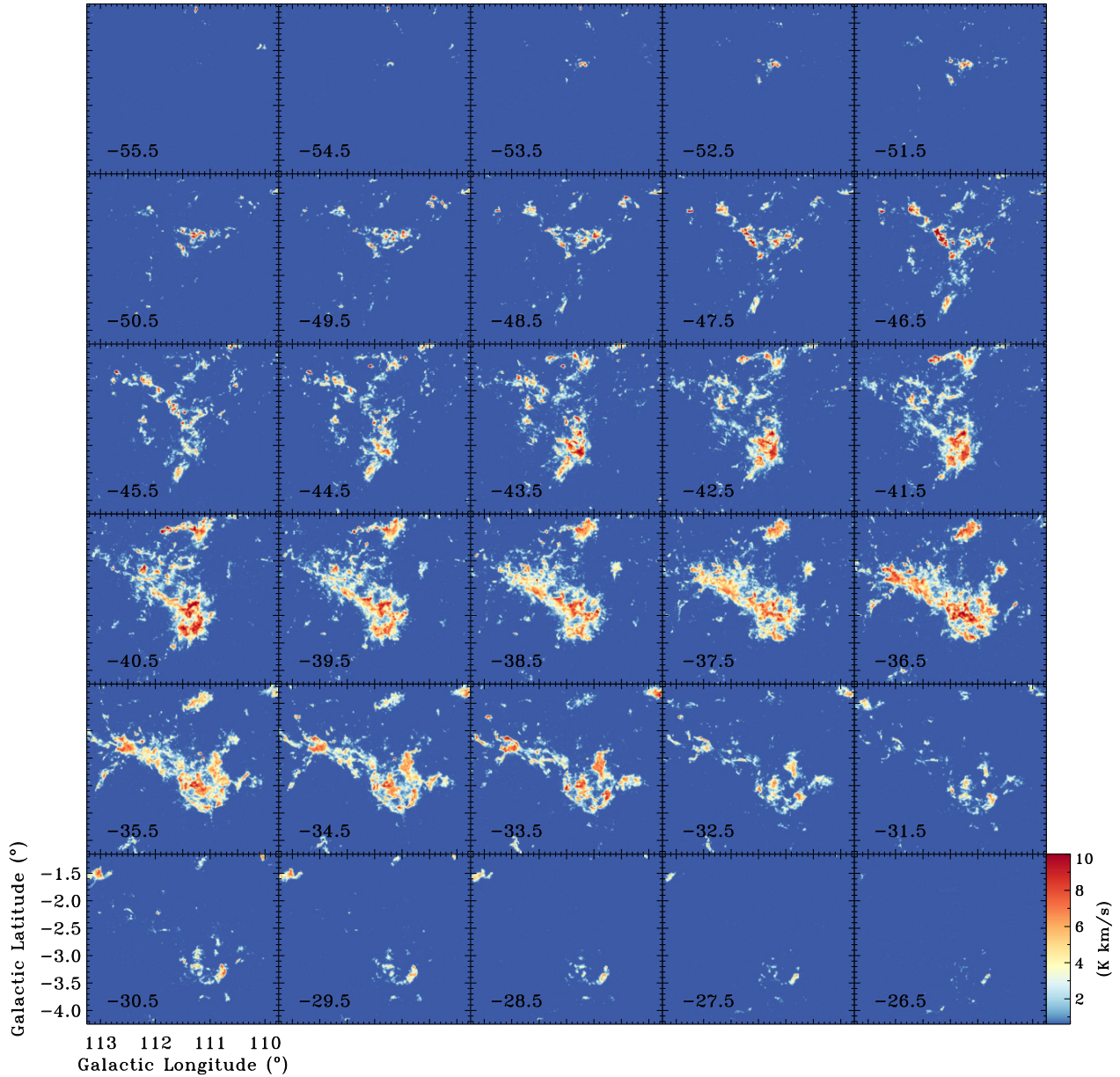


Figure 3. $^{12}\text{CO } J = 1 - 0$ velocity channel maps of the Cas GMC from -56 km s^{-1} to -26 km s^{-1} with a step of 1 km s^{-1} . The central velocity of each channel is shown at the bottom left corner of each panel.

of molecular clouds, the method with the Galactic rotation model will induce significant uncertainties in distance estimation. As the centroid velocities of Clouds 1-3 are consistent with the maser G111.25-00.76, we adopt a uniform distance of 3.4 kpc for the three main clouds 1-3 and the Cas GMC as a whole in the following calculations and discussions.

The column density of the clouds is calculated in two different ways. In the first way, we assume that the clouds are under the local thermodynamic equilibrium (LTE) conditions and the $^{12}\text{CO } J = 1 - 0$ emission is op-

tically thick. The excitation temperature is calculated with the peak intensity of the $^{12}\text{CO } J = 1 - 0$ emission, and the column density of ^{13}CO is calculated with the integrated intensity of the $^{13}\text{CO } J = 1 - 0$ emission. The detailed calculation processes are the same as in Li et al. (2018). The derived column density of ^{13}CO is then converted into the column density of molecular hydrogen with the abundance ratios $[^{12}\text{C}/^{13}\text{C}] = 6.21d_{GC} + 18.71$ and $\text{H}_2/^{12}\text{CO} = 1.1 \times 10^4$ (Frerking et al. 1982; Milam et al. 2005; Gong et al. 2016), where d_{GC} is the cloud distance from the Galactic center. In our case, the distance

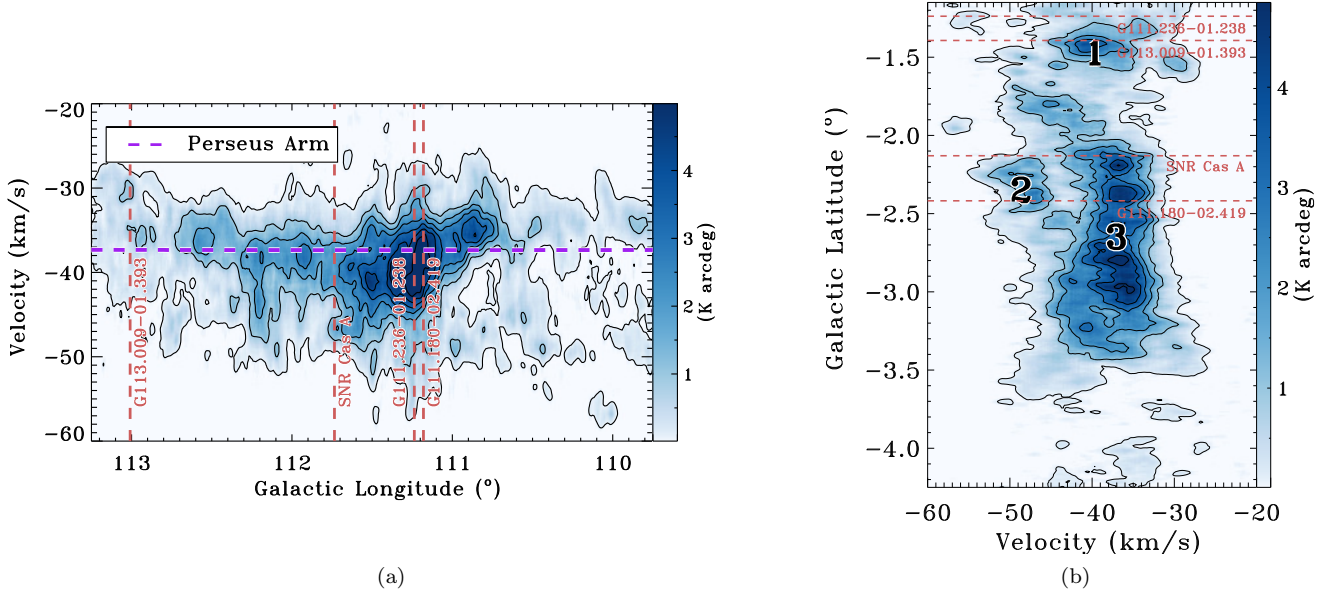


Figure 4. (a) ^{12}CO $l-v$ diagram. The purple dashed line is the $l-v$ curve for the Perseus Arm derived from model A5 from Reid et al. (2014). (b) Same as panel (a) but for the $b-v$ diagram. The numbers indicate the three PPV components of Cas GMC (see the text for detailed information). Red dashed lines in the two panels mark the positions of the H II regions and Cas A SNR. The contours start at 1.5σ and then increase to 0.8 times the emission peak in six steps that have the same intervals.

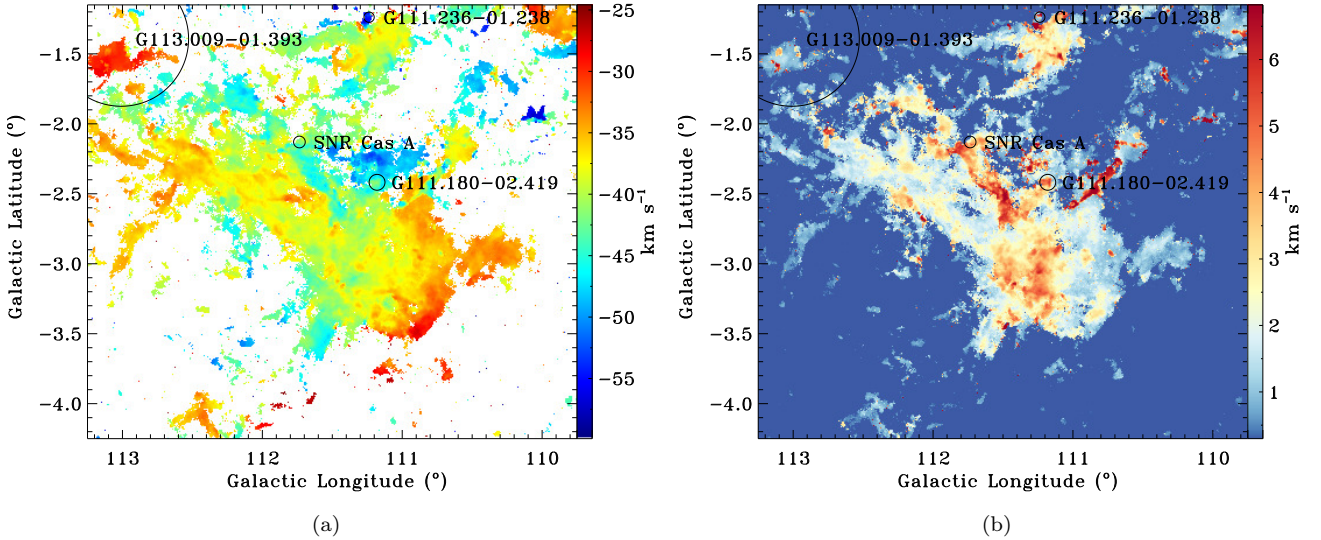


Figure 5. (a) Intensity-weighted centroid velocity map and (b) velocity dispersion map of the ^{12}CO emission over the velocity range from -60 to -24.5 km s^{-1} .

d_{GC} of the clouds is 10.1 kpc and the $^{12}\text{C}/^{13}\text{C}$ ratio is 81. In the second way, we use a constant conversion factor $X_{\text{CO}} = 2 \times 10^{20} \text{ cm}^{-2} (\text{K km s}^{-1})^{-1}$ (Bolatto et al. 2013) to convert the integrated intensity of ^{12}CO emission into the H_2 column density. The mass of the cloud is obtained through the integration of the H_2 column density over the effective emission area of the cloud.

The total mass for the whole Cas GMC derived using the LTE method from ^{13}CO is $2.1 \times 10^5 M_{\odot}$, and that using the X factor method is $9.5 \times 10^5 M_{\odot}$. The masses calculated with the above two methods and the average excitation temperatures for Clouds 1-3 are listed in Table 1. The masses of Clouds 1-3 lie between 10^4 and $10^5 M_{\odot}$. The X_{CO} masses are 3.7 to 6.7 times the LTE masses, which is common for Galactic GMCs.

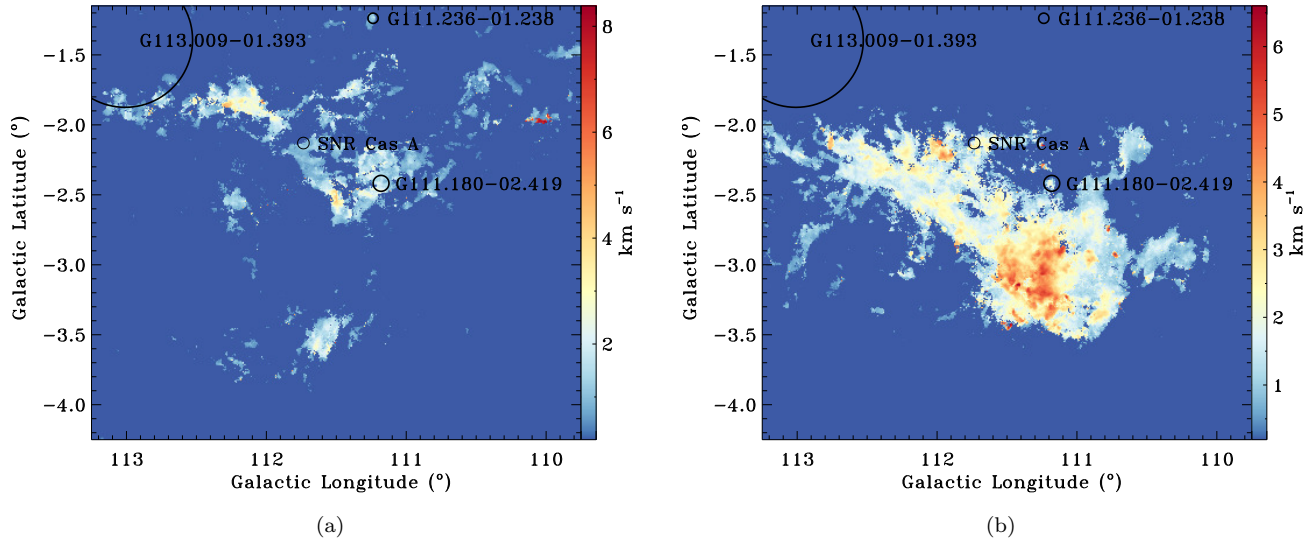


Figure 6. Velocity dispersion map of ^{12}CO emission of (a) Cloud 2 and (b) Cloud 3 in the velocity range from -60 to -24.5 km s^{-1} .

Table 1. Derived cloud parameters

Cloud	l_c ($^\circ$)	b_c ($^\circ$)	v_c (km s^{-1})	σ_v (km s^{-1})	d_{kin} (kpc)	T_{ex} (K)	M_{LTE} (M_\odot)	M_{XCO} (M_\odot)
Cloud 1	111.301	-1.454	-39.38	2.62	3.17	8.1	2.4×10^4	8.8×10^4
Cloud 2	111.578	-2.271	-46.13	2.46	3.73	7.4	2.4×10^4	1.6×10^5
Cloud 3	111.519	-2.770	-37.49	3.29	3.00	7.8	1.5×10^5	6.3×10^5

NOTE—Columns 2–4 give the centroid position and column 5 the velocity dispersion of the clouds. The velocity dispersion σ_v is derived from ^{13}CO data. The kinematic distance, the mean excitation temperature, and the mass of each cloud are given in Columns 6–9. Masses of the clouds are derived using a uniform distance of $d = 3.4$ kpc (see details in the text).

As introduced in Section 1, increasing temperature is one of the indicators of SNR-MC interaction and stellar feedback. We present the distribution and the statistics of the excitation temperature of the Cas GMC in Figure 7. The Cas GMC is generally cold, with a median temperature of about 7.5 K and a maximum of 20 K. No significant increase in temperature is found around the H II regions or the Cas A SNR except for two clumps at the southwestern edge of the H II region G113.009-01.393 and the ridge located below the SNR in the orientation of northeast-southwest. This ridge is part of Cloud 2. This temperature increase should be an intrinsic property of Cloud 2, rather than due to an interaction with the Cas A SNR. Therefore, the Cas GMC

is not affected by the Cas A SNR or H II regions at large scales in terms of increased temperature.

3.2. Interactions between the Cas A SNR and the GMC

3.2.1. Spectral Features

Observationally, there are several multiwavelength indicators for the diagnosis of SNR-MC interactions, such as the H_2 rovibrational lines and the [Fe II] emission line at the near infrared wavelength and the broadenings or the asymmetric profiles of the optically thin ^{12}CO rotational lines at the radio wavelength (Denoyer 1979; Dubner et al. 2004; Reach et al. 2005; Su et al. 2009; Zhou et al. 2009; Jiang et al. 2010; Chen et al. 2014; Kilpatrick et al. 2014; Su et al. 2017; Koo et al. 2018). In this work,

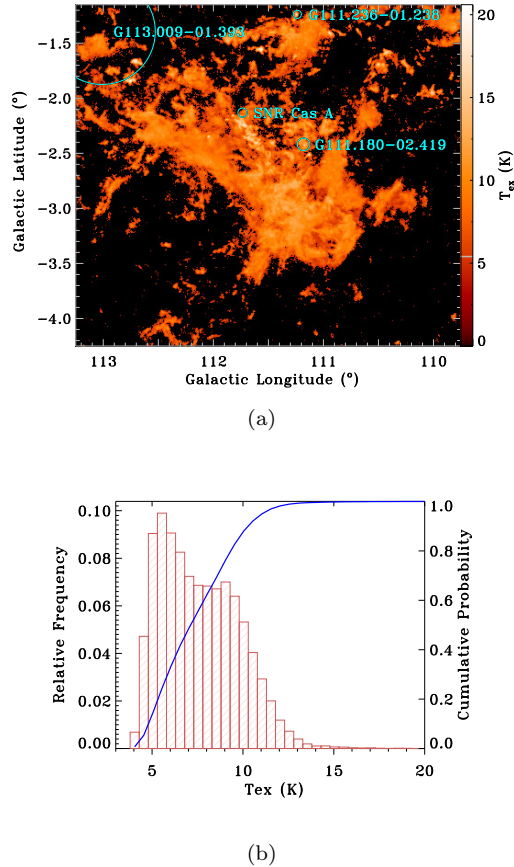


Figure 7. (a) Spatial distribution and (b) histogram of the excitation temperatures of the Cas GMC.

we manually examined all the $^{12}\text{CO } J = 1 - 0$ spectra for extra velocity broadenings or asymmetric wing emissions within a square region of $15' \times 15'$ centered at $\alpha(\text{J2000}) = 23^{\text{h}}23^{\text{m}}27.^{\text{s}}777$, $\delta(\text{J2000}) = 58^{\circ}48'49''.4$, i.e., the center of the Cas A SNR (Thorstensen et al. 2001). For the search of line broadenings, we use Gaussian fitting to get the FWHM velocities when the spectra have Gaussian profiles. We use the criterion $\Delta v > 6 \text{ km s}^{-1}$ (Kilpatrick et al. 2014) to screen out the broadened spectra.

We found some moderately broadened or asymmetric ^{12}CO lines in our examination. They are all limited to a $10' \times 10'$ region around the Cas A SNR, as indicated in Figure 8. Figure 9 gives the detailed line grid map of this region. As shown in Figure 9, lines at the the northwestern part of the region have more complex profiles than the southeastern lines. Two narrow velocity components occur in the southeastern lines, one with a centroid velocity of -47 km s^{-1} and the other with -37 km s^{-1} . Some positions near the center and to the southwest of the SNR have three narrow velocity components at -47 km s^{-1} , -42 km s^{-1} , and -37 km s^{-1} . The counter-

parts of the -37 km s^{-1} component in the northwestern lines are much broader than those in the southeastern and the southwestern lines. The lines that we found to be broadened or asymmetric can be further divided into five groups according to their locations in the region. For comparison, we also selected three control areas (6–8 in Figure 9). The spectra in these areas are characterized by narrow ^{12}CO lines. For convenience, we name the five areas with distinctive spectra and the three control areas as CO patches 1–8 hereafter. The polygons and the squares in Figures 8–9 serve to mark the locations of the CO patches 1–8.

The average spectra of CO patches 1–8 are present in Figure 10. In Figure 10, the ^{12}CO emission of the control areas, CO patches 6–8, consists of two velocity components, -47 km s^{-1} and -37 km s^{-1} , with the -47 km s^{-1} component being much stronger than the -37 km s^{-1} component. As shown in Figure 10, the line profiles of CO patches 1–5 are different from those of the CO patches 6–8. The spectra of CO patches 1–5 can be divided into three categories. The first category is represented by CO patches 1 and 5, which have one velocity component centered at -41 km s^{-1} and has wing emission extended toward both the red-shift and the blue-shift for about 7 km s^{-1} . However, the redshift wing of CO patch 1 is contaminated by another velocity component at -37 km s^{-1} . The spectra of CO patches 2 and 4 represent the second category, characterized by an asymmetric line profile with extended wing emission toward the red-shift. Nevertheless, the redshift wing of CO patch 2 is indistinguishable from the surrounding velocity components. The asymmetric profile of patch 4 is likely composed of two velocity components at -47 and -43 km s^{-1} . We have superimposed the Gaussian fittings of the two velocity components on the average spectrum of CO patch 4. The line width of the -43 km s^{-1} component is clearly larger than the counterpart of its spectra to the east and south of CO patch 4. Further, the -43 km s^{-1} velocity component also shows a Gaussian excess at the red-shift wing. Patch 3 represents the third category. We can see that the line widths of the two velocity components in CO patches 6–8 are all less than 3 km s^{-1} , but the -37 km s^{-1} component in CO patch 3 is broadened to 6.82 km s^{-1} , a factor of 2 larger than the the -37 km s^{-1} component in CO patches 6–8. The velocity of the ^{12}CO peak is red shifted relative to the ^{13}CO peak by about 2 km s^{-1} .

Kilpatrick et al. (2014) also found four regions with $^{12}\text{CO } J = 2 - 1$ line broadenings around the Cas A SNR, which are marked in Figure 8 and 9 with magenta circles “A” to “D.” Except for region C, the positions of the broadened $^{12}\text{CO } J = 2 - 1$ spectra do not coincide

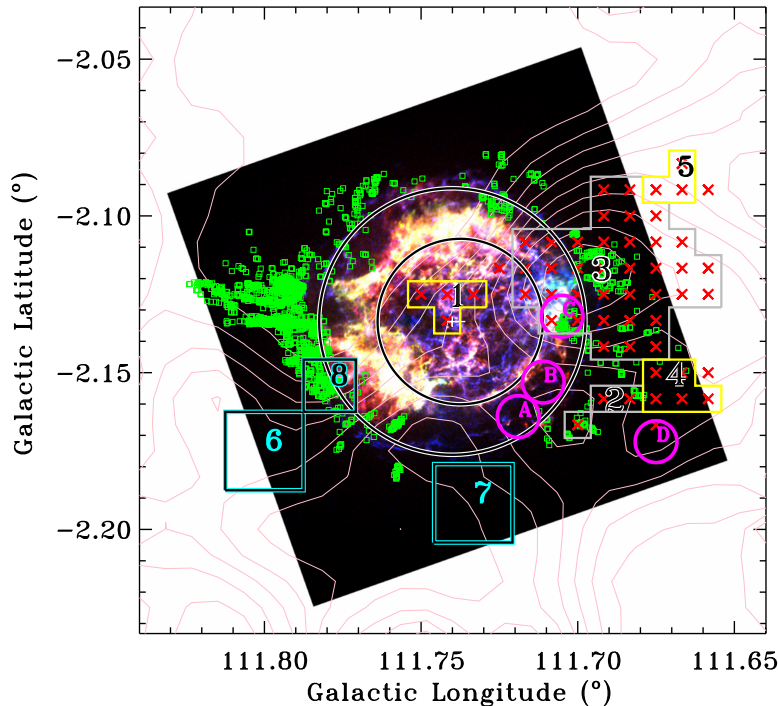


Figure 8. X-ray image of the Cas A SNR. The red, green, and blue colors correspond to the energy bands of 0.5–1.5, 1.5–3.5, and 4–6 KeV, respectively. The data are from the *Chandra X-ray Observatory* (http://chandra.harvard.edu/photo/openFITS/xray_data.html). The forward and the reverse shocks identified by [Gotthelf et al. \(2001\)](#) are represented with black circles. The pink contours represent ^{12}CO emission. The green squares designate the positions of the outer optical knots ([Hammell & Fesen 2008](#)). The red crosses indicate the positions with broadened or asymmetric $^{12}\text{CO } J = 1 - 0$ spectra that we found in this work. The gray and the yellow polygons mark the CO patches that show moderately broadened or asymmetric $^{12}\text{CO } J = 1 - 0$ spectra. The blue-black rectangles 6–8 mark the control regions. The positions of the broadened $^{12}\text{CO } J = 2 - 1$ spectra found by [Kilpatrick et al. \(2014\)](#) are shown with magenta circles.

with those of the broadened $^{12}\text{CO } J = 1 - 0$ spectra found in this work. For regions A and B, the -47 km s^{-1} velocity component of the $^{12}\text{CO } J = 2 - 1$ emission is mixed with the -37 km s^{-1} component. But in [Figure 9](#) we can see that the two velocity components in the $^{12}\text{CO } J = 1 - 0$ emission at the positions of A-D are separated, and no significant velocity broadenings are present. [Zhou et al. \(2018\)](#) also mapped the Cas A SNR with $^{12}\text{CO}/^{13}\text{CO } J = 1 - 0$ and $J = 2 - 1$ emission lines and searched for line broadening. They checked the spectra near the shock front, in the regions used in [Kilpatrick et al. \(2014\)](#), and at the positions of the CO brightness peaks. They did not find any prominent line broadening at these positions and proposed that the line widths of the spectra found by [Kilpatrick et al. \(2014\)](#) are not broader than those of the environment. They took $\Delta v > 10 \text{ km s}^{-1}$ as the criterion for significant line broadening, and they did not show the spectra at the

positions of CO patches 1, 4, and 5. Moreover, they searched for line broadenings at CO patch 3 by comparing the spectra in the pre- and postshocked regions. We note that in the CO patch 3 region there are many optical knots. These optical knots have very high velocities ($>10000 \text{ km s}^{-1}$) and carry a considerable amount of kinetic energy ([Hammell & Fesen 2008](#)). As was summarized by [Chevalier \(1977\)](#), the actual interaction between an SNR and its surrounding medium may show a combination of a smooth shell and some clumpy ejecta ([Figs 1 and 2](#) in their paper). When the clumpy ejecta interact with the surrounding medium, the bow shocks produced in front of them will change the dynamics of the surrounding gas. Therefore, it is possible that CO patches 3 and 4 have been disturbed by the Cas A SNR. CO patch 5 and the northwestern part of CO patch 3 are relatively far from the Cas A SNR, and they might be unreachable by the FMKs or the forward shock. The

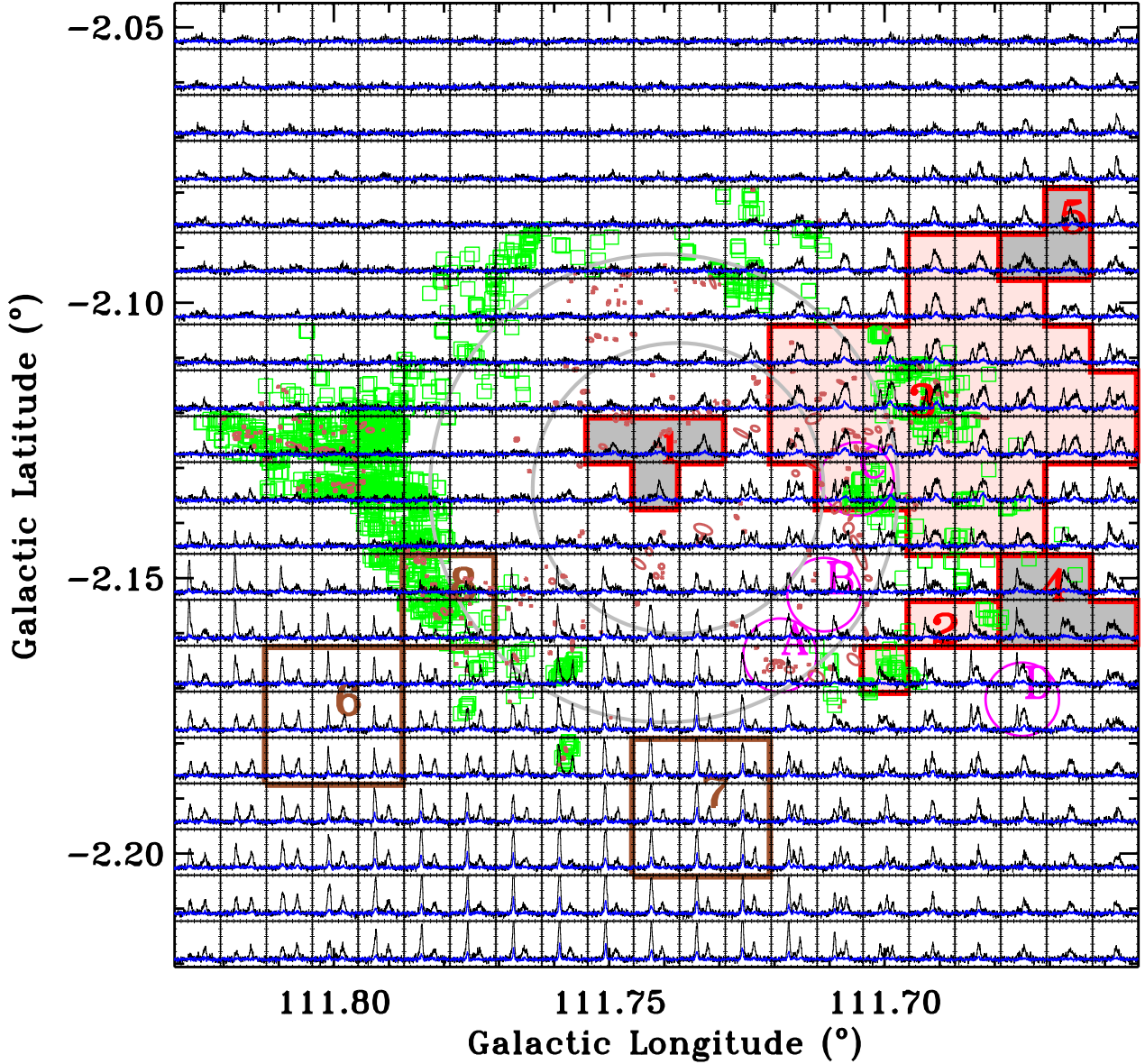


Figure 9. Line grid map of the $10' \times 10'$ region that we examined. The black and blue lines in each grid are the $^{12}\text{CO } J = 1 - 0$ and the $^{13}\text{CO } J = 1 - 0$ spectra, respectively. The circles, squares, and polygons are the same as in Figure 8. The adjacent polygons are filled with different colors for easy in distinguishing. The dark red ellipses are the NIR knots identified by Koo et al. (2018) in their deep [Fe II]+[Si I] map toward the Cas A SNR.

possible disturbing mechanisms for these regions are discussed in Section 3.2.2.

The SNR-MC interactions can also be observed in the near-infrared band. The shock-excited [Fe II] $1.64 \mu\text{m}$ emission is usually observed together with the H_2 $2.12 \mu\text{m}$ rovibrational lines in SNRs. It is found that the [Fe II] emission is often distributed close to but inside the H_2 NIR emission in SNRs (Reach et al. 2002; Lee et al. 2009). We have superimposed the [Fe II]+[Si I]

knots identified by Koo et al. (2018) in Figure 9 for comparison. Some [Fe II]+[Si I] knots spatially coincide with CO patches 1 and 3, but these knots cannot be taken as evidence for the SNR-MC interactions in this region, as Koo et al. (2018) found that the [Fe II]+[Si I] emission in this region is from the shocked dense atomic gas, rather than molecular gas. Due to the lack of other observational evidence such as increased temperature and the raised intensity ratio between CO $J = 2-1$ and $J=1-0$

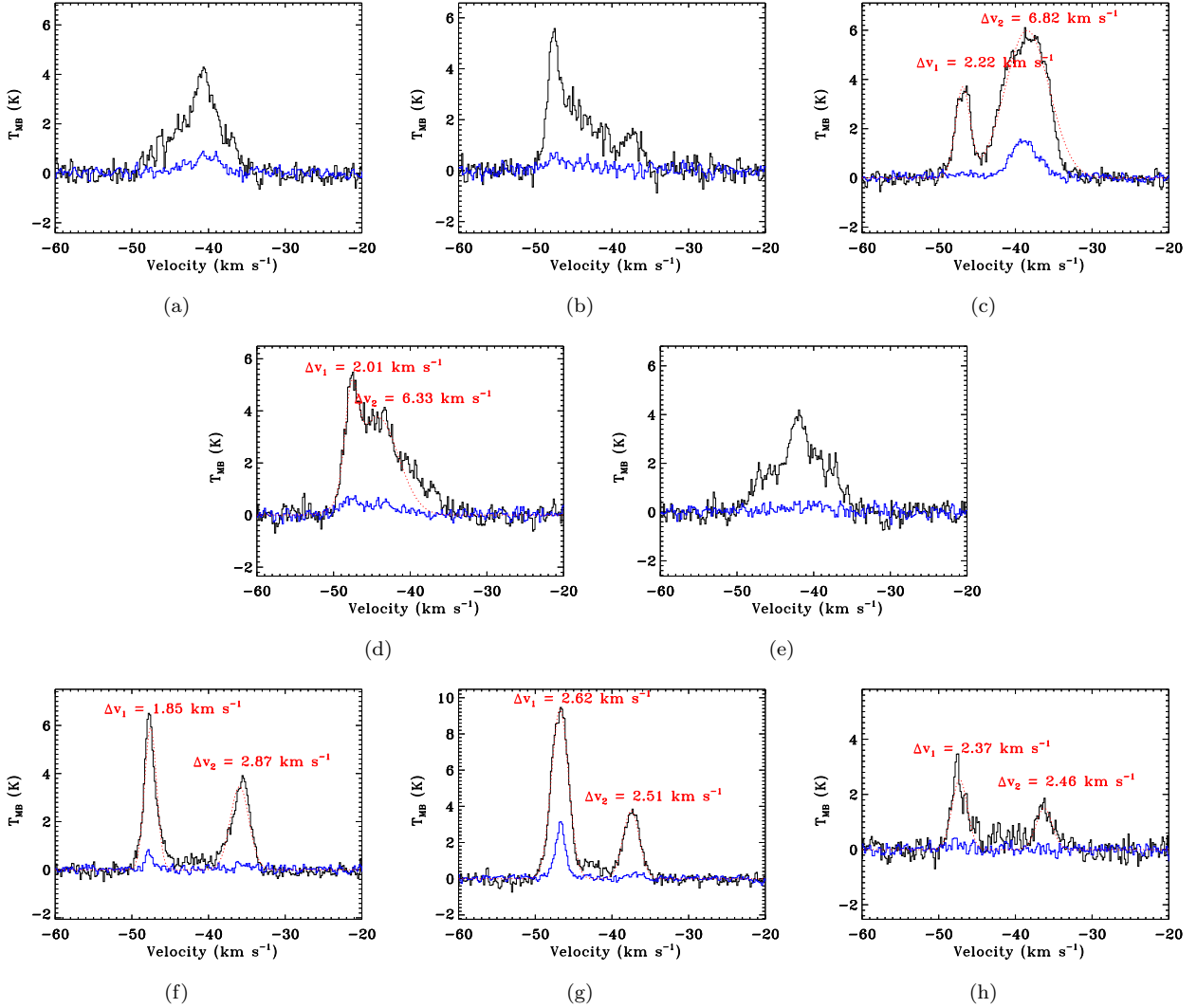


Figure 10. Average spectra of the disturbed regions and the comparison regions that are indicated in Figure 9, with panels (a) – (h) corresponding to regions 1–8. The black and blue spectra in each panel are the ^{12}CO and ^{13}CO $J = 1 - 0$ lines, respectively. For those regions with Gaussian-like line profiles, we fitted the ^{12}CO $J = 1 - 0$ line with gauss functions. The fitted profiles are plotted in red dotted lines, and the FWHM of each velocity component is given in the corresponding panel.

emission (Zhou et al. 2018), further proof is still needed for interactions in the region.

3.2.2. Large-Scale Kinematics of Molecular Gas around Cas A SNR

One advantage of our observation toward Cas A SNR compared with previous CO studies, such as those by Kilpatrick et al. (2014) and by Zhou et al. (2018), is the much larger sky coverage. The kinematics of the surrounding molecular gas can be investigated on a large scale. Outside the $10' \times 10'$ region (hereafter the central zone), there are four main clumpy structures in the velocity range of $v = [-44, -30]$ km s^{-1} . We have intercepted the $36' \times 30'$ area that covers the four main clumps and have created three moment maps for this subregion in the velocity range of $v = [-44, -30]$ km

s^{-1} . The results are displayed in Figure 11, where the four main clumps are marked clumps “a” to “d”. In the moment 0 map, it can be seen that the four clumps are located 2.5–13 pc away from the SNR center and that they encircle a less CO luminous region, which includes the southeast corner of the central zone. The moment 1 map reveals that all these clumps are blue-shifted by ~ 5 km s^{-1} relative to the center of the less luminous region, which forms a void-like structure in the position-velocity space. At the distance of the SNR, this velocity difference corresponds to a velocity gradient of about 0.6 $\text{km s}^{-1} \text{pc}^{-1}$. The velocity dispersions (moment 2) of these clumps are larger than the average velocity of the nearby clouds (see Figure 6(b)), and the values are as large as

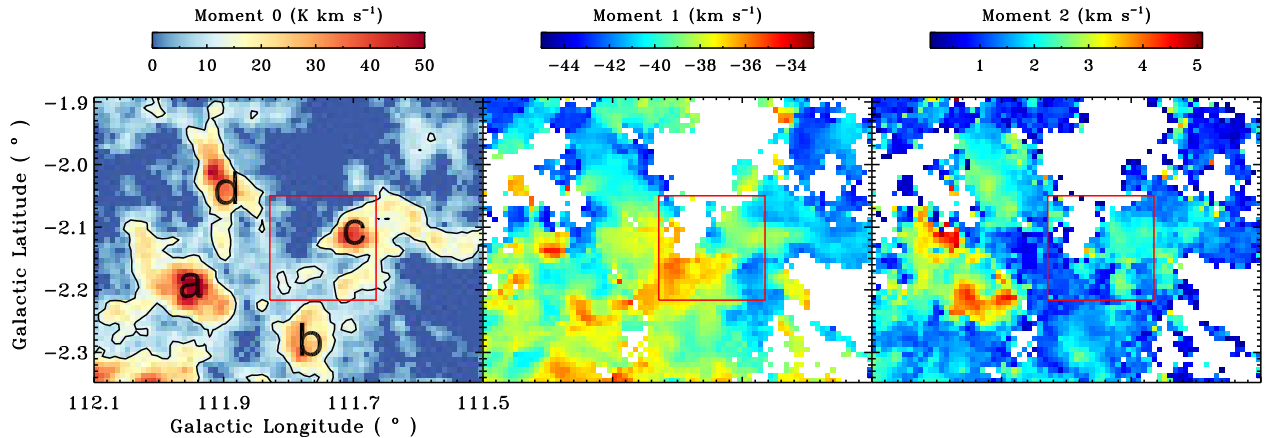


Figure 11. From left to right, the moment 0, 1, and 2 maps of a $36' \times 30'$ field centered on the SNR, showing the four clumps, a–d, at the vicinity of the Cas A SNR. In the first image, the black contour is 12 K km s^{-1} (15σ). The central $10' \times 10'$ region for which we have done the line fitting is indicated with the red rectangle.

5 km s^{-1} at the northeast and the southwest ends of clump a.

Although the clumps a, b, and d are far outside the forward shock front of the Cas A SNR, and thus they cannot be impacted by the ejecta of the Cas A SNR, it is interesting to explore the possible interaction between the wind from the progenitor of the Cas A SNR and these clumps. Although binary scenarios have been discussed for the progenitor of the Cas A SNR (Young et al. 2006), most authors argued that the progenitor is a single massive star with a ZAMS mass between 20 and $35 M_{\odot}$ (García-Segura et al. 1996; Pérez-Rendón et al. 2009; van Veelen et al. 2009). The progenitor may have experienced the main-sequence (MS), red supergiant (RSG), and Wolf-Rayet (W-R) evolution stages prior to the final explosion (García-Segura et al. 1996; Pérez-Rendón et al. 2009; van Veelen et al. 2009). The winds from the progenitor at the MS, RSG, and W-R stages can produce bubbles and inject energy to the surrounding medium. Following Whitworth et al. (1994), we use the analytic solution to calculate the radii of the bubbles produced by the winds (see equation 7 in their work). For the wind parameters, we use values given by stellar evolution models (García-Segura et al. 1996). We adopt a lifetime of $5 \times 10^6 \text{ yr}$, a mass-loss rate of $5 \times 10^{-7} M_{\odot} \text{ yr}^{-1}$, and a wind terminal velocity of 2000 km s^{-1} for the MS stage. When a number density of 10 cm^{-3} is used for the circumstellar material, the radius of the MS bubble is derived to be 38 pc. Even if a much higher density of the circumstellar matter, $n = 100 \text{ cm}^{-3}$, is used, the radius of the MS bubble is still up to 24 pc, which means that all the clumps a–d, including CO patch 5 and the northwestern part of CO patch 3, are in the reach of the MS wind of the pro-

genitor, if the clumps and the SNR are at the same distance. When we use the same number density $n = 10 \text{ cm}^{-3}$ for the circumstellar matter and the typical values of $\tau \sim 10^5 \text{ yr}$, $dM/dt \sim 10^{-4} M_{\odot} \text{ yr}^{-1}$, and $v = 50 \text{ km s}^{-1}$ for the RSG stage and $\tau \sim 10^4 \text{ yr}$, $dM/dt \sim 10^{-5} M_{\odot} \text{ yr}^{-1}$, $v = 1000 \text{ km s}^{-1}$ for the W-R stage (García-Segura et al. 1996), the radii of the RSG and W-R bubbles are 2.3 pc and 1.25 pc, respectively, which means that the clumps a, b, and d are well beyond the influence range of the RSG and W-R winds. Based on the aforementioned values for the wind parameters, the total kinetic energy that the MS wind has injected into the interstellar medium is $5 \times 10^6 M_{\odot} \text{ km}^2 \text{ s}^{-2}$ (corresponding to $1 \times 10^{50} \text{ erg}$). The masses of the CO clumps a–d are in the range of 2000–3200 M_{\odot} ; thus only 2–3 % of the injected energy from the MS wind is needed to cause a line broadening of 10 km s^{-1} for these clumps. For the eastern part of the CO patch 3 in clump c, which is close to the forward shock, its line broadening is likely caused by the influence of the SNR ejecta, because only 1% of the SN explosion energy ($\sim 10^{51} \text{ erg}$) or 10% of the FMKs’ kinetic energy ($\sim 10^{50} \text{ erg}$, Laming et al. 2006) is capable of a 10 km s^{-1} broadening for a cloud with mass as large as $10^4 M_{\odot}$.

3.3. Properties of ^{13}CO Clumps

In this section, we decompose the Cas GMC into a set of clumps and discuss their statistical and dynamical properties.

3.3.1. Method and Calculation

Kramer et al. (1998) present a brief review of the different methods for decomposing molecular clouds into discrete clumps, from by-eye inspection to auto-

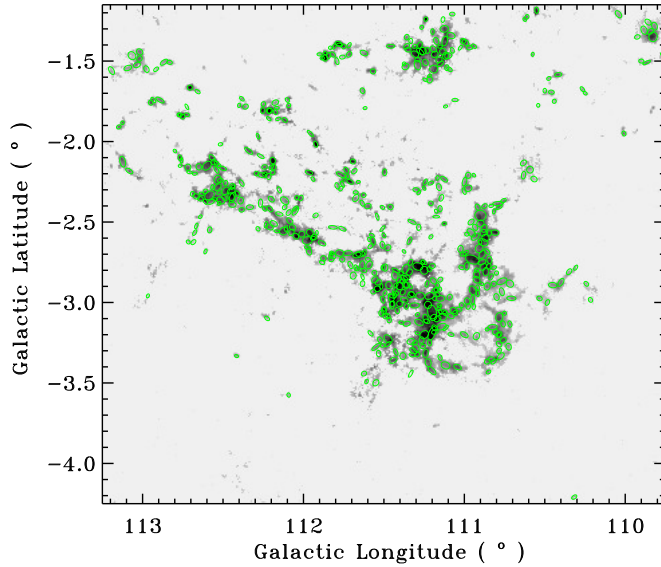


Figure 12. Spatial distribution of the ^{13}CO clumps identified in the Cas GMC using the GAUSSCLUMPS algorithm. The background is the column density distribution of the Cas GMC, and the green ellipses represent the fitted clumps.

mated clump-finding algorithms, such as the widely used GAUSSCLUMPS (Stutzki & Guesten 1990) and CLUMPFIND (Williams et al. 1994). Williams et al. (1994) suggested that both GAUSSCLUMPS and CLUMPFIND perform well in identifying intermediate-to high-mass clumps, whereas GAUSSCLUMPS can avoid velocity blending. To avoid velocity blending, we therefore chose to use the GAUSSCLUMPS task in GILDAS software to identify ^{13}CO clumps in this work. We used the following settings in the calculation, $T = 1.61$ K (7σ) for the termination temperature, $(s_0, s_a, s_c) = (1, 1, 1)$ for the stiffness parameters, and 3 (in units of velocity or spatial resolution) for the FWHMs of the weighting function. The stiffness parameters confine the peak temperature and the peak position of a fitted clump. The FWHMs are used to make sure that the Gaussian fitting in each iteration actually uses the data points that are physically related to the observed peak position. The method for the column density calculation has been discussed in Section 3.1.2. Here we only give a brief description of the calculation of the other parameters of the detected clumps. The mass of a clump is obtained through its total ^{13}CO flux, $T_{peak}\Delta v\theta_a\theta_b[\pi/(4\ln 2)]^{3/2}$, where Δv , θ_a , and θ_b are the FWHM along each axis of a triaxial gaussian clump. The effective radius of a clump is obtained through the deconvolution of the fitted clump size, $R_{eff} = 1/2d(\theta_a\theta_b - \theta_{beam}^2)^{1/2}$ (Stutzki & Guesten 1990), where θ_{beam} is the HPBW of the PMO-13.7 m telescope and $d = 3.4$ kpc is the distance of the Cas

GMC. The surface density and volume number density of the clump are then derived as $\Sigma = M/(\pi R_{eff}^2)$ and $n(\text{H}_2) = 3M/(4\pi R_{eff}^3\mu m_H)$, respectively.

3.3.2. Statistical Properties of the Clumps

In this work, we ignore the clumps that have fitted angular sizes smaller than $1.5\theta_{beam}$. Ultimately, we identified 547 ^{13}CO clumps in total. The spatial distribution of these clumps is displayed in Figure 12. Table 2, as an example, lists the physical parameters from the GAUSSCLUMPS algorithm and also the derived parameters for some clumps. The whole table for all identified clumps is available in machine-readable format.

The most widely used indicator of the equilibrium state of a molecular clump is the virial parameter (Bertoldi & McKee 1992),

$$\alpha = \frac{5\sigma_v^2 R}{GM} \approx 209 \left(\frac{R}{\text{pc}} \frac{\Delta v^2}{\text{km s}^{-1}} \frac{M_\odot}{M_{LTE}} \right) \quad (1)$$

where σ_v is the velocity dispersion of the fitted clump, which is related to Δv via $\Delta v = \sqrt{8\ln 2}\sigma_v$. The virial parameter measures the ratio between the internal kinetic energy and the gravitational energy. A clump with virial parameter $\alpha > \alpha_{cr}$ is subcritical, which will expand or need external pressure to be confined, while a clump with virial parameter $\alpha < \alpha_{cr}$ is supercritical, which will collapse under its self-gravity. In the simplest equilibrium analysis of molecular clumps that only considers internal pressure and gravity, the result of $\alpha_{cr} = 1$ is obtained. When detailed models of stability

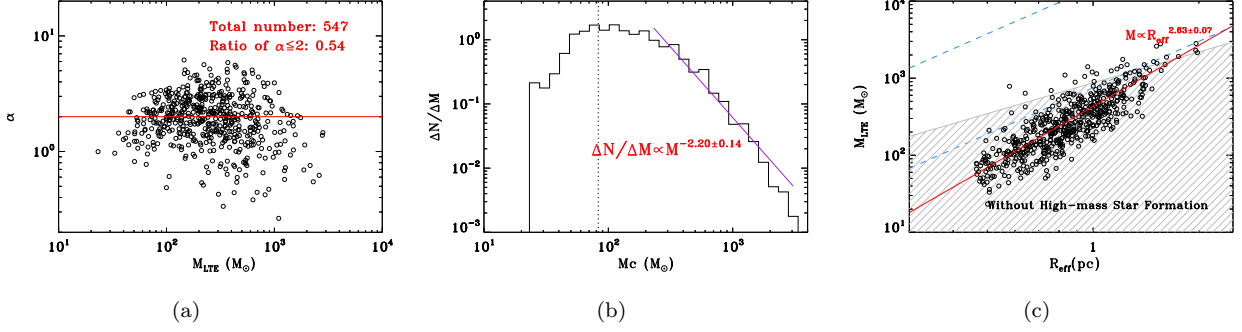


Figure 13. (a) Relationship between the virial parameters and the masses of the clumps. The red horizontal line indicates $\alpha_{vir} = 2$. The total number of the clumps and the fraction of the clumps with α_{vir} no larger than 2 are shown in the top-right corner in this panel. (b) Clump Mass Function (CMF) of the Cas GMC. The purple line indicates the power-law fitting of the CMF with an index of -2.20 . The vertical dashed line marks the detection limit derived from the settings used in the GAUSSCLUMPS algorithm. (c) M–R relation of the clumps. The shaded area is the region where the clump masses follow the empirical relationship $M(R) = 870M_{\odot}(r/pc)^{1.33}$ found by [Kauffmann et al. \(2010a\)](#). The blue dotted lines indicate the empirical upper and lower bounds of the clump surface density of 1 g cm^{-2} and 0.05 g cm^{-2} for massive star formation ([Urquhart et al. 2013](#))

and the response of models to perturbations are considered, the critical value for a nonmagnetized isothermal hydrostatic equilibrium sphere is $\alpha_{cr} = 2$ ([Kauffmann et al. 2013](#)). Figure 13(a) shows that 54% of the clumps are supercritical and are unstable to collapse unless they are supported by other forces, such as magnetic fields.

No correlation between the virial parameters and masses of the clumps is found in Figure 13(a). By comparison, [Bertoldi & McKee \(1992\)](#) and [Kauffmann et al. \(2013\)](#) found an anticorrelation, $\alpha \propto M^{h_{\alpha}}$, for the pressure-confined clumps (with an index $h_{\alpha} = -2/3$) and the supercritical clumps in high-mass star forming regions.

Table 2. Properties of ^{13}CO clumps

Name	l	b	θ_a	θ_b	PA	v_{lsr} (km s^{-1})	T_{peak} (K)	Δv (km s^{-1})	R_{eff} (pc)	T_{ex} (K)	τ	N_{H_2} cm^{-2}	M_{LTE} (M_\odot)	Σ ($M_\odot \text{pc}^{-2}$)	n	α_{vir}
MWISP G109.758-01.475-048.48	109.758	-1.475	82	82	-74	-48.48	1.8	0.67	0.5	10.1	0.3	8.6×10^{20}	4.0×10^1	4.4×10^1	8.8×10^2	1.27
MWISP G109.767-01.459-051.14	109.767	-1.459	76	109	139	-51.14	1.9	0.93	0.6	10.0	0.3	1.3×10^{21}	7.3×10^1	5.8×10^1	9.9×10^2	1.57
MWISP G109.818-01.283-034.86	109.818	-1.283	122	178	107	-34.86	3.0	1.15	1.1	10.1	0.6	2.8×10^{21}	4.3×10^2	1.0×10^2	9.8×10^2	0.74
MWISP G109.827-01.349-033.55	109.827	-1.349	188	217	80	-33.55	3.8	1.96	1.6	10.2	0.8	6.7×10^{21}	1.9×10^3	2.3×10^2	1.5×10^3	0.69
MWISP G109.843-01.316-033.38	109.843	-1.316	106	159	41	-33.38	2.0	1.05	1.0	9.9	0.4	1.5×10^{21}	1.8×10^2	5.8×10^1	6.4×10^2	1.27
MWISP G109.858-01.258-034.70	109.858	-1.258	109	158	138	-34.70	1.8	1.01	1.0	10.1	0.3	1.3×10^{21}	1.6×10^2	4.9×10^1	5.3×10^2	1.38
MWISP G109.867-01.509-046.99	109.867	-1.509	62	187	26	-46.99	1.9	1.93	0.8	9.7	0.4	2.6×10^{21}	2.1×10^2	1.1×10^2	1.5×10^3	2.90
MWISP G109.883-01.308-033.37	109.883	-1.308	130	192	111	-33.37	1.8	1.66	1.2	9.2	0.4	2.1×10^{21}	3.6×10^2	7.4×10^1	6.5×10^2	2.01
MWISP G109.900-01.500-048.98	109.900	-1.500	116	88	-5	-48.98	2.0	1.28	0.7	9.8	0.4	1.8×10^{21}	1.3×10^2	7.6×10^1	1.1×10^3	1.96
MWISP G109.925-01.350-031.88	109.925	-1.350	128	95	20	-31.88	1.7	1.08	0.8	9.4	0.3	1.3×10^{21}	1.1×10^2	5.1×10^1	6.8×10^2	1.86
MWISP G110.008-01.950-056.45	110.008	-1.950	83	115	110	-56.45	4.5	0.94	0.7	16.6	0.4	4.6×10^{21}	3.0×10^2	2.0×10^2	3.1×10^3	0.43
MWISP G110.042-01.209-030.22	110.042	-1.209	111	183	128	-30.22	2.1	1.39	1.1	8.6	0.5	2.1×10^{21}	2.9×10^2	7.5×10^1	7.4×10^2	1.54
MWISP G110.216-02.984-034.87	110.216	-2.984	90	112	121	-34.87	2.1	0.73	0.7	7.8	0.6	1.1×10^{21}	7.7×10^1	4.7×10^1	7.0×10^2	1.05
MWISP G110.242-02.884-034.04	110.242	-2.884	86	121	132	-34.04	1.7	1.45	0.7	10.1	0.3	1.7×10^{21}	1.2×10^2	7.3×10^1	1.1×10^3	2.60
MWISP G110.249-01.700-049.81	110.249	-1.700	96	68	-34	-49.81	2.2	0.91	0.5	10.9	0.3	1.5×10^{21}	6.8×10^1	7.7×10^1	1.6×10^3	1.35
MWISP G110.266-01.675-049.48	110.266	-1.675	72	134	130	-49.48	2.9	0.94	0.7	11.4	0.4	2.2×10^{21}	1.5×10^2	9.6×10^1	1.5×10^3	0.87
MWISP G110.308-02.784-036.53	110.308	-2.784	69	128	57	-36.53	1.7	1.70	0.7	10.6	0.3	2.1×10^{21}	1.3×10^2	9.3×10^1	1.5×10^3	3.12
MWISP G110.317-04.209-037.20	110.317	-4.209	77	131	35	-37.20	2.1	1.07	0.7	8.8	0.5	1.6×10^{21}	1.1×10^2	6.9×10^1	1.0×10^3	1.53
MWISP G110.349-02.809-036.03	110.349	-2.809	95	151	51	-36.03	1.8	1.23	0.9	10.8	0.3	1.7×10^{21}	1.7×10^2	6.5×10^1	7.9×10^2	1.71
MWISP G110.400-02.875-034.87	110.400	-2.875	103	200	58	-34.87	1.6	2.36	1.1	10.0	0.3	2.6×10^{21}	3.7×10^2	9.6×10^1	9.4×10^2	3.48
MWISP G110.417-01.584-049.14	110.417	-1.584	159	91	6	-49.14	3.5	1.55	0.9	15.9	0.3	5.4×10^{21}	5.4×10^2	2.1×10^2	2.5×10^3	0.84
MWISP G110.441-01.750-049.81	110.441	-1.750	86	93	63	-49.81	2.2	1.02	0.6	10.3	0.4	1.7×10^{21}	9.4×10^1	7.8×10^1	1.4×10^3	1.43
MWISP G110.450-02.892-034.20	110.450	-2.892	117	194	174	-34.20	1.9	1.66	1.2	8.9	0.4	2.2×10^{21}	3.5×10^2	8.0×10^1	7.4×10^2	1.96
MWISP G110.459-01.693-049.15	110.459	-1.693	90	126	169	-49.15	3.8	0.83	0.8	11.2	0.6	2.8×10^{21}	2.2×10^2	1.1×10^2	1.6×10^3	0.51
MWISP G110.475-01.608-048.98	110.475	-1.608	80	100	30	-48.98	1.8	1.53	0.6	11.5	0.3	2.2×10^{21}	1.2×10^2	1.0×10^2	1.8×10^3	2.53
MWISP G110.484-03.000-034.04	110.484	-3.000	88	136	64	-34.04	1.7	1.51	0.8	9.9	0.3	1.8×10^{21}	1.5×10^2	7.4×10^1	1.0×10^3	2.52
MWISP G110.500-01.684-049.48	110.500	-1.684	78	104	92	-49.48	2.8	0.61	0.6	17.2	0.2	1.8×10^{21}	1.0×10^2	8.2×10^1	1.4×10^3	0.49
MWISP G110.533-02.975-034.53	110.533	-2.975	122	101	-20	-34.53	2.0	1.63	0.8	10.3	0.3	2.4×10^{21}	2.1×10^2	9.8×10^1	1.3×10^3	2.20
MWISP G110.541-01.775-046.32	110.541	-1.775	71	83	88	-46.32	2.0	0.71	0.5	10.9	0.3	1.1×10^{21}	4.5×10^1	6.0×10^1	1.4×10^3	1.14
MWISP G110.549-01.916-045.66	110.549	-1.916	56	138	151	-45.66	2.0	1.00	0.6	12.0	0.3	1.6×10^{21}	8.4×10^1	7.4×10^1	1.4×10^3	1.49
MWISP G110.551-01.184-042.68	110.551	-1.184	83	141	94	-42.68	2.3	3.62	0.8	10.7	0.4	6.5×10^{21}	5.2×10^2	2.6×10^2	3.6×10^3	4.17

NOTE—The source name is defined under the MWISP standard. Columns 2–6 give the centroid positions, the FWHMs of the two principal axes, and the position angles of the clumps. The centroid velocity, the peak intensity of ^{13}CO emission, and the FWHM line width of the clumps are presented in columns 7–9. Columns 10–17 list the derived parameters of the clumps, i.e., effective radius, excitation temperature, optical depth, H_2 column density, total mass derived from the LTE method, surface density, number density, and the virial parameter, respectively. This table is available in its entirety in machine-readable form.

The mass distribution, ranging from about $20 M_{\odot}$ to $3 \times 10^3 M_{\odot}$, of the identified clumps is displayed in Figure 13(b). Previously, clumps identified using different methods and on different scales exhibit a universal power-law mass spectrum, $dN/dM \propto M^{-\alpha}$, with a power-law index α ranging from 1.4 to 2.2 (Blitz 1993; Rice et al. 2016). The power-law index of the clump mass function (CMF) is very sensitive to the fit range. We fit the CMF from the mass derived with the median values of all the physical parameters to the mass end of the histogram in Figure 13(b). The resulting power-law index is 2.20. This value is similar to the that of the CMF of the molecular clouds in the outer galaxy (2.2) (Rice et al. 2016), but is larger than the indexes (1.6–1.8) found by Kramer et al. (1998). A CMF index greater than 2.0 indicates that the majority of the mass of clumps is contained in the low-mass clumps.

The relation between the masses and the sizes of clumps is a probe of the density distribution of cloud fragments (Kauffmann et al. 2010a,b). Kauffmann et al. (2010a) studied the mass-radius relation of clumps in several solar neighborhood clouds and found that clouds with masses under the empirical relationship $M(R) \leq 870 M_{\odot} (R/pc)^{1.33}$ are not capable of hosting massive star formation (see shaded area in Figure 13(c)). Figure 13(c) also shows the empirical upper and lower bounds of the clump surface density, 1 g cm^{-2} and 0.05 g cm^{-2} , required for massive star formation (Urquhart et al. 2013). Almost all clumps identified in this work fall below the Kauffmann’s relation and the lower bound surface density of 0.05 g cm^{-2} (corresponds to $1.07 \times 10^{22} \text{ cm}^{-2}$). This result is consistent with the lack of ongoing massive star formation in this region. The red line in Figure 13(c) shows the power-law fit of the mass-size relation $M \propto R_{eff}^{2.63}$ of the clumps. With a power-law index of 2.63, this result indicates the non-uniform surface densities of clumps on parsec scales.

Figure 14(a) shows the distribution of the velocity dispersions of the identified clumps. The observed velocity dispersions range from 0.2 km s^{-1} to 1.7 km s^{-1} , with a median value around 0.6 km s^{-1} . Larson (1981) found a line-width–size relation $\sigma_v \propto R_{eff}^{0.38}$ for molecular clouds and suggested that the internal turbulence of the clouds is responsible for this relation. The fitted line-width–radius relation for the clumps identified in this work is shown with the red solid line in Figure 14(b). The exponent is 0.54, larger than the Larson’s exponent of 0.38, but the Pearson correlation coefficient of $\log R_{eff}$ and $\log \sigma_v$ is low (0.42). Figure 14(c) gives the relationship between σ_v^2/R_{eff} and the surface density Σ of the clumps. We can see that σ_v^2/R_{eff} varies systematically with Σ , which is similar to the result found by

Heyer et al. (2009). This relationship conflicts with the Larson’s third law that molecular clouds have constant surface densities. Our results indicate that the internal motions of molecular clouds depend both on their sizes and surface densities. The solid and dashed purple lines in Figure 14(c) show the relationships corresponding to simple virial equilibrium (SVE; $\alpha = 1$) and marginally bound clouds ($\alpha = 2$), respectively. The majority of the identified clumps are distributed above the SVE line but along the marginally bound line ($\alpha = 2$), which implies that gravity plays a dominant role in confining the identified clumps. This result is different from that obtained in the OGS survey, where Heyer et al. (2001) found that external pressure is needed to confine the clouds.

4. DISCUSSION

4.1. Probability Density Function (PDF) of the Column Density

The column density PDF (N-PDF) is a simple but very useful tool to describe the molecular cloud structure. Both theoretical work and numerical simulations predict that the N-PDFs of molecular clouds are characterized by log-normal functions when supersonic turbulence is the dominant dynamical process in molecular clouds and the N-PDFs tend to develop power-law tails at high densities once self-gravity becomes important (Vazquez-Semadeni 1994; Padoan et al. 1997; Klessen 2000; Federrath et al. 2010). This evolutionary trend has been supported by a broad range of observations with different kinds of tracers of column density (Goodman et al. 2009; Kainulainen et al. 2009; Schneider et al. 2013). However, Tassis et al. (2010) have shown through numerical simulations that log-normal N-PDFs are generic features of diverse model clouds that do not include supersonic turbulence, and they suggested that log-normal N-PDFs should not be interpreted as being a consequence of supersonic turbulence. Alves et al. (2017) argued that no log-normal PDFs are present if the completeness (the last closed contour of the sample) of the observation is taken into account. The wide-field survey toward the Cas GMC allows us to examine the N-PDF in this region.

Figure 15(a) displays the spatial distribution of the H_2 column density derived from the LTE method. The corresponding pixel-by-pixel N-PDF is shown in Figure 15(b). According to Alves et al. (2017), the last closed contour has a decisive role in determining the reliability of the log-normal peak. The completeness of our statistics is reflected in Figure 15(a) with the black contour, which corresponds to the detection limit. We note that none of the molecular cloud samples used in the study of Alves et al. (2017) were fully covered by ob-

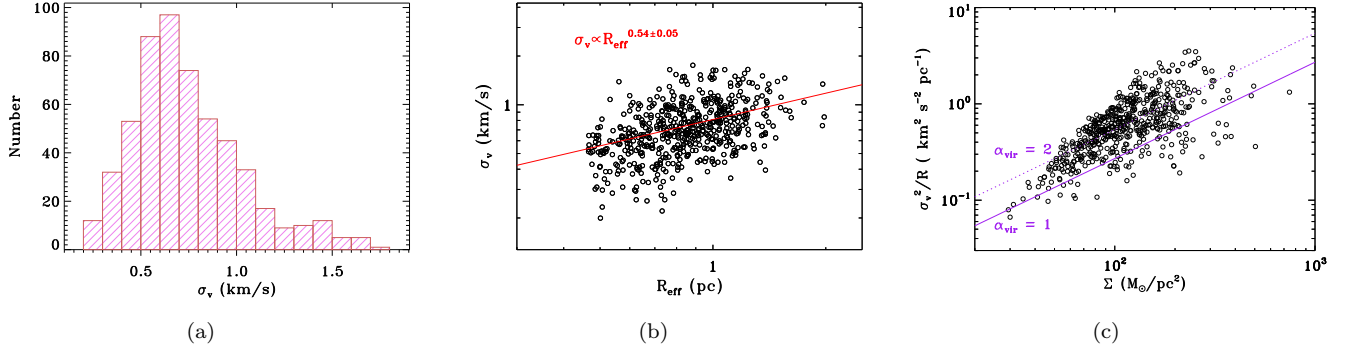


Figure 14. (a) Distribution of velocity dispersion, (b) line-width–size relation, and (c) σ_v^2/R vs. surface density for the fitted ^{13}CO clumps in the Cas GMC.

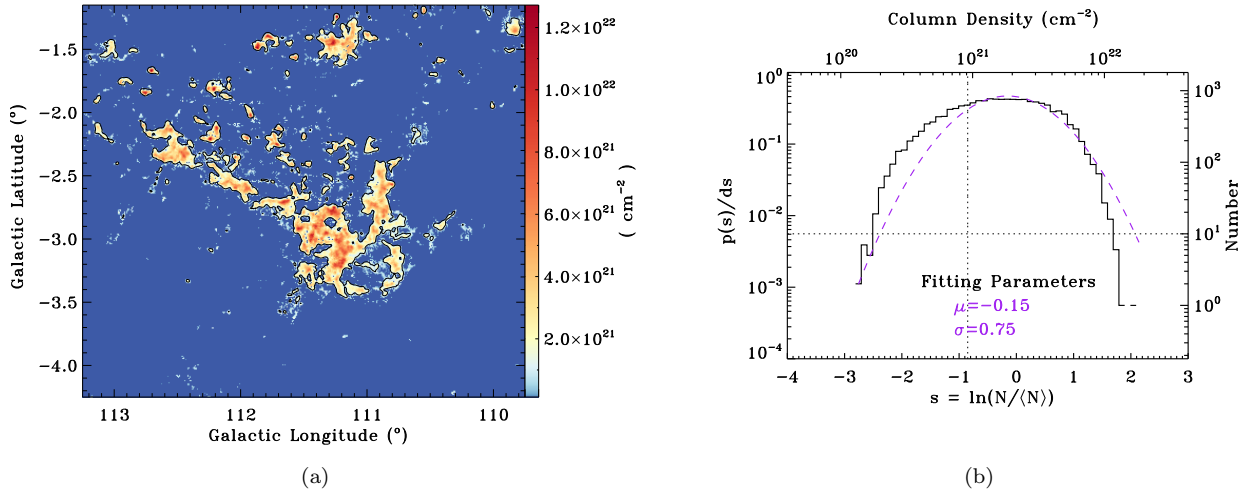


Figure 15. (a) Spatial distribution of the column density in Cas GMC derived under the assumption of LTE. (b) Probability density function of the H_2 column density of Cas GMC. The vertical and horizontal dashed lines mark the detection limit and where the number of pixels within a bin is 10, respectively. μ and σ are the mean and dispersion of the fitted Gaussian function of $\ln(N/\langle N \rangle)$.

servations. In this work, our observations fully cover the Cas GMC. We fit the PDF with a log-normal function from the detection limit $N_{\text{H}_2} = 9.2 \times 10^{20} \text{cm}^{-2}$ to $N_{\text{H}_2} = 1.1 \times 10^{22} \text{cm}^{-2}$ which is the value of the last bin that has the number of pixels greater than 10. The N-PDF can be well fitted in the range from $\sim 10^{21} \text{cm}^{-2}$ to $\sim 10^{22} \text{cm}^{-2}$ but drops drastically toward high densities when $N_{\text{H}_2} > 10^{22} \text{cm}^{-2}$. The overall column density of the GMC is low, with an average column density of $N_{\text{H}_2} = 1.6 \times 10^{21} \text{cm}^{-2}$, which is much below the threshold of star formation $6.3 \times 10^{21} \text{cm}^{-2}$ (Johnstone et al. 2004; Lada et al. 2010; Kainulainen et al. 2014). The absence of a power tail at the high column density end in this region is consistent with the fact that this GMC is quiescent in star formation (see discussions in Section 4.2). These results all show that the Cas GMC is either in

its early evolutionary stage or has passed its main star formation phase.

4.2. Star Formation in the Cas GMC

To investigate the star formation activity in the Cas GMC, we used the archive data of WISE and 2MASS to identify young stellar objects (YSOs). The YSO identification scheme resembles the one described in Koenig et al. (2012). The detailed criteria can be found in Koenig & Leisawitz (2014). Here we just give a brief description of the identification process. Firstly, for the sources with detections in the WISE W1, W2, and W3 bands, the Class I and Class II YSOs are identified based on their infrared excess after the contamination of star-forming galaxies and AGNs is removed. Second, YSOs are identified among the remaining sources based on infrared excess in the $H-K_s$ versus $W1-W2$ color space.

Thirdly, the WISE W4 ($22\ \mu\text{m}$) photometry is used to identify transition disks and to retrieve protostars from the AGN candidates. Finally, all YSOs identified above are re-examined to exclude the possible asymptotic giant branch (AGB) and classical Be stars (CBe) (Rivinius et al. 2013).

We totally identified 21 Class I protostars and 76 Class II YSOs in this region. The spatial distribution of the identified Class I and Class II YSOs is presented in Figure 2. Overall, most of the YSOs are associated with (i.e., no farther than 5 pc from) the Cas GMC if we assume the YSOs are at the same distance as the Cas GMC. Because no information on the distances of the identified YSOs is available at present, we also checked the possible association between the YSOs and the local gas. The result shows poor association between them. Compared with the Cas GMC, the local gas in this region is much less. Therefore, it is reasonable to assume that the YSOs in this region are born in the Cas GMC.

Overall, the distribution of YSOs in this region does not show obvious clustering, only somewhat concentrated near the H II regions G113.009–01.393 and G111.236–01.236 and the western arc-shaped structure of Cloud 3. Compared with YSOs in the H II regions, YSOs in the western arc-shaped structure of Cloud 3 are associated more closely with molecular gas, where the column density of the gas is close to or slightly larger than the threshold of star formation, $N_{\text{H}_2} \sim 6.3 \times 10^{21}\ \text{cm}^{-2}$. Half of the total LTE mass of the Cas GMC has column density below $3 \times 10^{21}\ \text{cm}^{-2}$ and only 12% of the total mass has column density above the star formation threshold. The first value is comparable to that for the Taurus molecular cloud (TMC; $2.1 \times 10^{21}\ \text{cm}^{-2}$) (Goldsmith et al. 2008), which is a nearby dark cloud inactive in star formation. Assuming an average YSO mass of $0.5\ M_{\odot}$, we calculated the star formation efficiency (SFE) of the Cas GMC to be 0.02% when we use the LTE mass of $2.1 \times 10^5\ M_{\odot}$. Considering the large distance of Cas GMC and the sensitivity of the WISE survey, the YSO sample we have obtained is not complete. The value of 0.02% is a lower limit of the actual star formation efficiency of the GMC. By comparison, this value is far below the SFE of the TMC (0.3–1.2%) (Goldsmith et al. 2008) and that of the Ophiuchus north cloud (0.3%) (Nozawa et al. 1991). This may be a result of the lack of high-density gas in the Cas GMC.

5. SUMMARY

We have conducted a fully covered simultaneous survey of the ^{12}CO , ^{13}CO , and $\text{C}^{18}\text{O}\ J = 1 - 0$ emission toward the Cas A SNR with a sky coverage of $3.5^{\circ} \times 3.1^{\circ}$. The GMC in this region is nearly free of C^{18}O emission,

and its ^{12}CO and ^{13}CO emission comes from molecular gas with velocity in the range from -55 to $-25\ \text{km s}^{-1}$. The spatial distribution and velocity structures of the GMC are revealed for the first time. The main results are presented as follows.

1. The total mass of the Cas GMC is $2.1 \times 10^5\ M_{\odot}$ as derived from the ^{13}CO emission and $9.5 \times 10^5\ M_{\odot}$ from the ^{12}CO emission. The GMC can be divided into three main clouds with masses on the order of 10^4 – $10^5\ M_{\odot}$ based on the spatial and velocity distribution. Combined with the parallax distance information of two adjacent galactic masers, G111.23–01.23 and G111.25–00.76, we propose a distance of $d = 3.4\ \text{kpc}$ for the Cas GMC.
2. Two regions with broadened (6 – $7\ \text{km s}^{-1}$) or asymmetric ^{12}CO line profiles are found in the vicinity of the Cas A SNR (within a $10' \times 10'$ region). The criterion of line broadening is $\Delta v > 6\ \text{km s}^{-1}$. At distances of 2.5 – $13\ \text{pc}$ from the Cas A SNR center, we have identified four clumps with masses in the range of 2000 to $3200\ M_{\odot}$ that encompass a less luminous cavity around the Cas A SNR. The southeastern clump, clump a, shows velocity dispersions as large as $5\ \text{km s}^{-1}$. All the four clumps possess velocity gradients toward the southeast corner of the SNR. The velocity gradients and the large velocity dispersions may be caused by the influence of the MS wind of the progenitor of the Cas A SNR.
3. Using the GAUSSCLUMPS algorithm, we have identified 547 ^{13}CO clumps in the GMC, 54% of which are found to be gravitationally bound ($\alpha < 2$). The CMF of the clumps follows a power-law distribution with an exponent of -2.20 . The mass-radius relation $M \propto R_{eff}^{2.63}$ of the clumps is inconsistent with the Larson’s third law of constant surface density and suggests non-uniform internal density distribution. The values of σ_v^2/R_{eff} values of the clumps vary systematically with the surface densities.
4. The pixel-by-pixel distribution of the H_2 column density of the GMC can be well fitted with a log-normal PDF. The median value of the H_2 column density of the GMC is $1.6 \times 10^{21}\ \text{cm}^{-2}$ and half the mass of the GMC is contained in regions with H_2 column density lower than $3 \times 10^{21}\ \text{cm}^{-2}$, which is well below the column density threshold of star formation (Johnstone et al. 2004). The distribution of the YSO candidates in the region shows no agglomeration. The lack of high-density gas in the

Cas GMC is consistent with its low SFE of 0.02%, which is much lower than those of the two typical inactive star formation clouds, the Taurus and the Ophiuchus north regions.

We thank the PMO-13.7 m telescope staff for their supports during the observation and the anonymous referee for constructive suggestions. This work is supported by the National Key R&D Program of China (NO. 2017YFA0402701). We acknowledge the support by NSFC grants 11233007, 11127903, and 11503086. Y.M. acknowledges the support by NSFC grant 11503087 and by the Natural Science Foundation of Jiangsu Province of China (grant No. BK20141046). M.Z. acknowledges the support of funding from the European Unions Horizon 2020 research and innovation program under grant agreement No. 639459 (PROMISE). We credit NASA/CXC/SAO for the X-ray FITS images of the Cas A SNR. This publication makes use of data products from the *Wide-field Infrared Survey Explorer*, which is a joint project of the University of California, Los Angeles, and the Jet Propulsion Laboratory/California Institute of Technology, funded by the National Aeronautics and Space Administration. This publication also makes use of data products from the Two Micron All Sky Survey, which is a joint project of the University of Massachusetts and the Infrared Processing and Analysis Center/California Institute of Technology, funded by the National Aeronautics and Space Administration and the National Science Foundation. This work makes use of the SIMBAD database, operated at CDS, Strasbourg, France.

Software: GILDAS/CLASS (Pety 2005; Gildas Team 2013)

6. APPENDIX

We present the velocity channel maps, p-v diagrams, and moment 1 and 2 maps of the $^{13}\text{CO } J = 1 - 0$ emission in Figures 16–18, respectively.

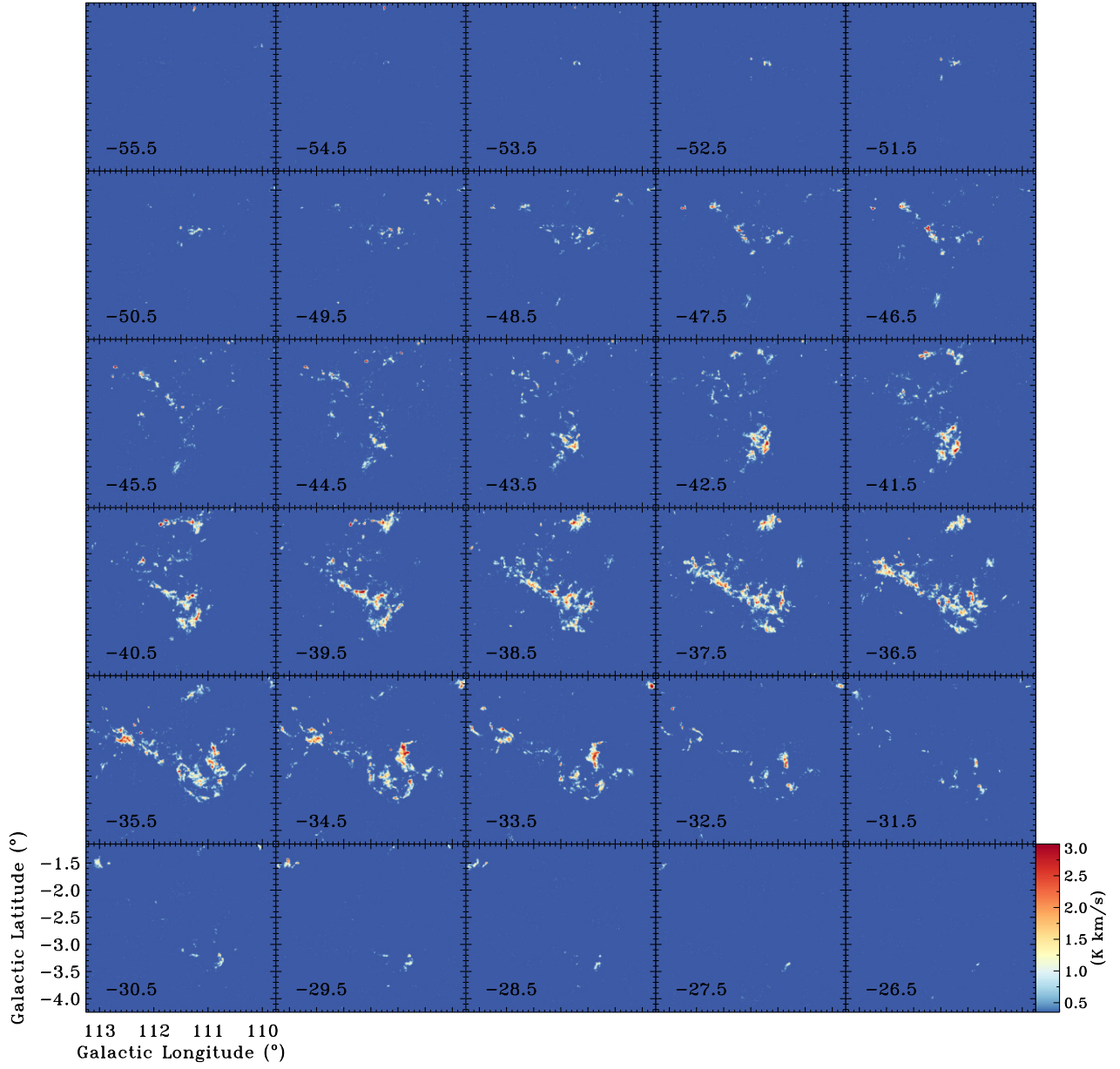


Figure 16. $^{13}\text{CO } J=1-0$ velocity channel maps of Cas GMC integrated from -56 km s^{-1} to -26 km s^{-1} per 1 km s^{-1} . The central velocity of the integral interval is shown at the lower-left corner in each panel.

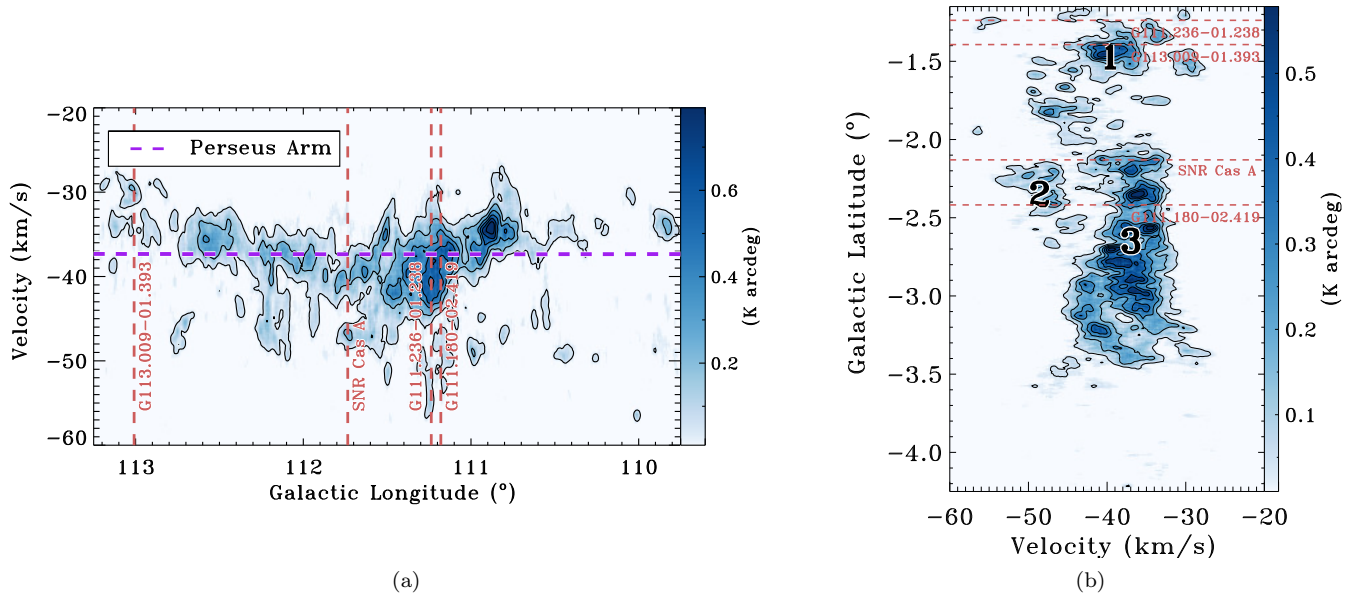


Figure 17. Same as Figure 4 but with ^{13}CO emission.

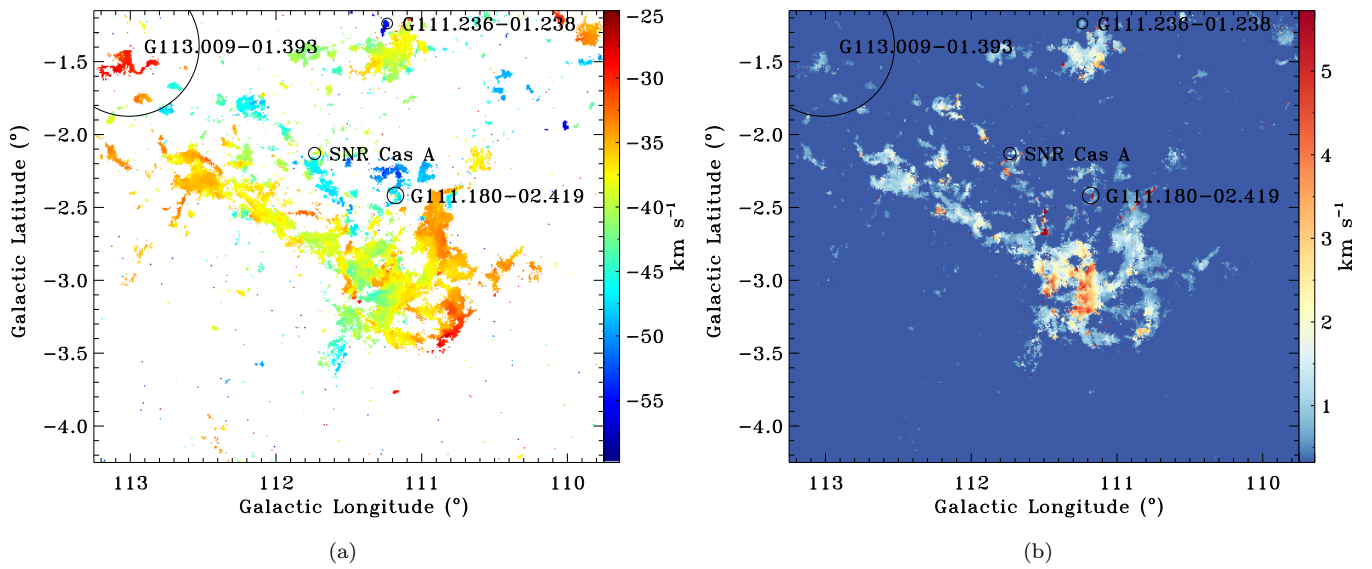


Figure 18. Same as Figure 5 but with ^{13}CO emission.

REFERENCES

- Alves, J., Lombardi, M., & Lada, C. J. 2017, *A&A*, 606, L2
- Anderson, L. D., Bania, T. M., Balsler, D. S., et al. 2014, *ApJS*, 212, 1
- Arce, H. G., Borkin, M. A., Goodman, A. A., Pineda, J. E., & Beaumont, C. N. 2011, *ApJ*, 742, 105
- Bally, J. 2016, *ARA&A*, 54, 491
- Bertoldi, F., & McKee, C. F. 1992, *ApJ*, 395, 140
- Bieging, J. H., & Crutcher, R. M. 1986, *ApJ*, 310, 853
- Blitz, L. 1993, in *Protostars and Planets III*, ed. E. H. Levy & J. I. Lunine, 125–161
- Blitz, L., & Williams, J. P. 1999, *ArXiv Astrophysics e-prints*, astro-ph/9903382
- Bolatto, A. D., Wolfire, M., & Leroy, A. K. 2013, *ARA&A*, 51, 207
- Chen, Y., Jiang, B., Zhou, P., et al. 2014, in *IAU Symposium*, Vol. 296, *Supernova Environmental Impacts*, ed. A. Ray & R. A. McCray, 170–177
- Chevalier, R. A. 1977, *ARA&A*, 15, 175
- Dame, T. M., Hartmann, D., & Thaddeus, P. 2001, *ApJ*, 547, 792
- Denoyer, L. K. 1979, *ApJL*, 232, L165
- Dubner, G., Giacani, E., Reynoso, E., & Parón, S. 2004, *A&A*, 426, 201
- Ennis, J. A., Rudnick, L., Reach, W. T., et al. 2006, *ApJ*, 652, 376
- Falgarone, E., & Perault, M. 1987, in *NATO ASIC Proc. 210: Physical Processes in Interstellar Clouds*, ed. G. E. Morfill & M. Scholer, 59–73
- Federrath, C., Roman-Duval, J., Klessen, R. S., Schmidt, W., & Mac Low, M.-M. 2010, *A&A*, 512, A81
- Fesen, R. A., & Gunderson, K. S. 1996, *ApJ*, 470, 967
- Fesen, R. A., Zastrow, J. A., Hammell, M. C., Shull, J. M., & Silvia, D. W. 2011, *ApJ*, 736, 109
- Fesen, R. A., Hammell, M. C., Morse, J., et al. 2006, *ApJ*, 645, 283
- Ferking, M. A., Langer, W. D., & Wilson, R. W. 1982, *ApJ*, 262, 590
- García-Segura, G., Langer, N., & Mac Low, M.-M. 1996, *A&A*, 316, 133
- Gildas Team. 2013, *GILDAS: Grenoble Image and Line Data Analysis Software*, *Astrophysics Source Code Library*, , , ascl:1305.010
- Goldsmith, P. F., Heyer, M., Narayanan, G., et al. 2008, *ApJ*, 680, 428
- Gong, Y., Mao, R. Q., Fang, M., et al. 2016, *A&A*, 588, A104
- Goodman, A. A., Pineda, J. E., & Schnee, S. L. 2009, *ApJ*, 692, 91
- Goss, W. M., Kalberla, P. M. W., & Dickel, H. R. 1984, *A&A*, 139, 317
- Gotthelf, E. V., Koralesky, B., Rudnick, L., et al. 2001, *ApJL*, 552, L39
- Green, D. A. 2014, *Bulletin of the Astronomical Society of India*, 42, 47
- . 2017, *VizieR Online Data Catalog*, 7278
- Hammell, M. C., & Fesen, R. A. 2008, *ApJS*, 179, 195
- Heyer, M., & Dame, T. M. 2015, *ARA&A*, 53, 583
- Heyer, M., Krawczyk, C., Duval, J., & Jackson, J. M. 2009, *ApJ*, 699, 1092
- Heyer, M. H., Brunt, C., Snell, R. L., et al. 1998, *ApJS*, 115, 241
- Heyer, M. H., Carpenter, J. M., & Snell, R. L. 2001, *ApJ*, 551, 852
- Jiang, B., Chen, Y., Wang, J., et al. 2010, *ApJ*, 712, 1147
- Johnstone, D., Di Francesco, J., & Kirk, H. 2004, *ApJL*, 611, L45
- Kainulainen, J., Beuther, H., Henning, T., & Plume, R. 2009, *A&A*, 508, L35
- Kainulainen, J., Federrath, C., & Henning, T. 2014, *Science*, 344, 183
- Kauffmann, J., Pillai, T., & Goldsmith, P. F. 2013, *ApJ*, 779, 185
- Kauffmann, J., Pillai, T., Shetty, R., Myers, P. C., & Goodman, A. A. 2010a, *ApJ*, 716, 433
- . 2010b, *ApJ*, 712, 1137
- Kilpatrick, C. D., Bieging, J. H., & Rieke, G. H. 2014, *ApJ*, 796, 144
- Klessen, R. S. 2000, *ApJ*, 535, 869
- Koenig, X. P., & Leisawitz, D. T. 2014, *ApJ*, 791, 131
- Koenig, X. P., Leisawitz, D. T., Benford, D. J., et al. 2012, *ApJ*, 744, 130
- Koo, B.-C., Kim, H.-J., Lee, Y.-H., et al. 2018, *ApJ*, 866, 139
- Kramer, C., Stutzki, J., Rohrig, R., & Corneliussen, U. 1998, *A&A*, 329, 249
- Krause, O., Birkmann, S. M., Usuda, T., et al. 2008, *Science*, 320, 1195
- Lada, C. J., Lombardi, M., & Alves, J. F. 2010, *ApJ*, 724, 687
- Laming, J. M., Hwang, U., Radics, B., Lekli, G., & Takács, E. 2006, *ApJ*, 644, 260
- Larson, R. B. 1981, *MNRAS*, 194, 809
- Lee, H.-G., Moon, D.-S., Koo, B.-C., Lee, J.-J., & Matthews, K. 2009, *ApJ*, 691, 1042
- Lee, J.-J., Park, S., Hughes, J. P., & Slane, P. O. 2014, *ApJ*, 789, 7
- Li, C., Wang, H., Zhang, M., et al. 2018, *ApJS*, 238, 10

- Massaro, F., D'Abrusco, R., Landoni, M., et al. 2015, *ApJS*, 217, 2
- Matzner, C. D. 2002, *ApJ*, 566, 302
- Milam, S. N., Savage, C., Brewster, M. A., Ziurys, L. M., & Wyckoff, S. 2005, *ApJ*, 634, 1126
- Nozawa, S., Mizuno, A., Teshima, Y., Ogawa, H., & Fukui, Y. 1991, *ApJS*, 77, 647
- Padoan, P., Nordlund, A., & Jones, B. J. T. 1997, *MNRAS*, 288, 145
- Patnaude, D. J., & Fesen, R. A. 2014, *ApJ*, 789, 138
- Pérez-Rendón, B., García-Segura, G., & Langer, N. 2009, *A&A*, 506, 1249
- Pety, J. 2005, in *SF2A-2005: Semaine de l'Astrophysique Française*, ed. F. Casoli, T. Contini, J. M. Hameury, & L. Pagani, 721
- Reach, W. T., Rho, J., & Jarrett, T. H. 2005, *ApJ*, 618, 297
- Reach, W. T., Rho, J., Jarrett, T. H., & Lagage, P.-O. 2002, *ApJ*, 564, 302
- Reed, J. E., Hester, J. J., Fabian, A. C., & Winkler, P. F. 1995, *ApJ*, 440, 706
- Reid, M. J., Menten, K. M., Brunthaler, A., et al. 2014, *ApJ*, 783, 130
- Reynoso, E. M., & Goss, W. M. 2002, *ApJ*, 575, 871
- Rice, T. S., Goodman, A. A., Bergin, E. A., Beaumont, C., & Dame, T. M. 2016, *ApJ*, 822, 52
- Rivinius, T., Carciofi, A. C., & Martayan, C. 2013, *A&A Rv*, 21, 69
- Scalo, J. M. 1985, in *Protostars and Planets II*, ed. D. C. Black & M. S. Matthews, 201–296
- Schneider, N., André, P., Könyves, V., et al. 2013, *ApJL*, 766, L17
- Seta, M., Hasegawa, T., Dame, T. M., et al. 1998, *ApJ*, 505, 286
- Shan, W., Yang, J., Shi, S., et al. 2012, *IEEE Transactions on Terahertz Science and Technology*, 2, 593
- Solomon, P. M., Rivolo, A. R., Barrett, J., & Yahil, A. 1987, *ApJ*, 319, 730
- Stutzki, J., & Guesten, R. 1990, *ApJ*, 356, 513
- Su, Y., Chen, Y., Yang, J., et al. 2009, *ApJ*, 694, 376
- Su, Y., Zhou, X., Yang, J., et al. 2017, *ApJ*, 836, 211
- Su, Y., Yang, J., Zhang, S., et al. 2019, *ApJS*, 240, 9
- Tassis, K., Christie, D. A., Urban, A., et al. 2010, *MNRAS*, 408, 1089
- Thorstensen, J. R., Fesen, R. A., & van den Bergh, S. 2001, *AJ*, 122, 297
- Truelove, J. K., & McKee, C. F. 1999, *ApJS*, 120, 299
- Ungerechts, H., Umbanhowar, P., & Thaddeus, P. 2000, *ApJ*, 537, 221
- Urquhart, J. S., Moore, T. J. T., Schuller, F., et al. 2013, *MNRAS*, 431, 1752
- van Veelen, B., Langer, N., Vink, J., García-Segura, G., & van Marle, A. J. 2009, *A&A*, 503, 495
- Vázquez-Semadeni, E. 1994, *ApJ*, 423, 681
- Whitworth, A. P., Bhattal, A. S., Chapman, S. J., Disney, M. J., & Turner, J. A. 1994, *MNRAS*, 268, 291
- Williams, J. P., Blitz, L., & Stark, A. A. 1995, *ApJ*, 451, 252
- Williams, J. P., de Geus, E. J., & Blitz, L. 1994, *ApJ*, 428, 693
- Wilson, T. L., Mauersberger, R., Muders, D., Przewodnik, A., & Olano, C. A. 1993, *A&A*, 280, 221
- Young, P. A., Fryer, C. L., Hungerford, A., et al. 2006, *ApJ*, 640, 891
- Zhou, P., Li, J.-T., Zhang, Z.-Y., et al. 2018, *ApJ*, 865, 6
- Zhou, X., Chen, Y., Su, Y., & Yang, J. 2009, *ApJ*, 691, 516